Undersampled Phase Retrieval With Outliers

Daniel S. Weller, *Member, IEEE*, Ayelet Pnueli, Gilad Divon, Ori Radzyner, Yonina C. Eldar, *Fellow, IEEE*, and Jeffrey A. Fessler, *Fellow, IEEE*

***Abstract*—This paper proposes a general framework for reconstructing sparse images from undersampled (squared)-magnitude data corrupted with outliers and noise. This phase retrieval method uses a layered approach, combining repeated minimization of a convex majorizer (surrogate for a nonconvex objective function), and iterative optimization of that majorizer using a preconditioned variant of the alternating direction method of multipliers (ADMM). Since phase retrieval is nonconvex, this implementation uses multiple initial majorization vectors. The introduction of a robust 1-norm data fit term that is better adapted to outliers exploits the generality of this framework. The derivation also describes a normalization scheme for the regularization parameter and a known adaptive heuristic for the ADMM penalty parameter. Both 1-D Monte Carlo tests and 2-D image reconstruction simulations suggest the proposed framework, with the robust data fit term, reduces the reconstruction error for data corrupted with both outliers and additive noise, relative to competing algorithms having the same total computation.**

***Index Terms*—Phase retrieval, sparsity, majorize-minimize, alternating direction method of multipliers.**

I. Introduction

PHASE retrieval [1]–[3] refers to the problem of recovering a signal or image from magnitude-only measurements of a transform of that signal. This problem appears in crystallography [4]–[7], optics [8], astronomy [9], and other areas [10]–[14].

Phase retrieval is inherently ill-posed, as many signals may share the same magnitude spectrum [15]. To address this issue, existing phase retrieval algorithms incorporate different sources of prior information. The Gerchberg-Saxton error reduction method [16] of alternating projections uses magnitude information about both an image and its Fourier spectrum. Fienup's hybrid input-output algorithm [17], [18] generalizes the image domain projection of error reduction to other constraints such as image boundary and support information [19]–[24]. More recently, the alternating projections framework [25] has been extended to sparse reconstruction [26]–[28]; examples include compressive phase retrieval [29], the message-passing method PR-GAMP [30], and the sparse Fienup method [31]. Other formulations approach phase retrieval differently. One method uses rough phase estimates [32] to dramatically improve reconstruction quality. Another uses a matrix lifting scheme [33], [34] to construct a semidefinite relaxation of the phase retrieval problem [35] that may be combined with sparsity-promoting regularization [33], [36]–[41]. Graph-based and convex optimization methods in [42] and greedy algorithms like GESPAR [43] also employ sparsity for phase retrieval.

Measurements can be very noisy at the resolution desired in many phase retrieval imaging applications. Many existing methods either ignore measurement noise or use quadratic data fit terms. The proposed method, based on [44], employs a robust 1-norm data fit term, corresponding to the negative log-likelihood of a Laplace distribution, to improve robustness to outliers. This data fit term can also be found in some matrix lifting phase retrieval methods [40], [41], at the expense of much larger memory and computational resources. Fast convergence of the proposed reconstruction can be achieved through a new optimization framework nesting two iterative components: alternating direction method of multipliers (ADMM) iterations inside each step of an outer majorize-minimize (MM) algorithm. This framework accommodates both the desired 1-norm data fit term and sparsity-promoting regularization. More specifically, majorization yields a tight convex surrogate for the original nonconvex objective. Introducing an auxiliary variable enables efficient minimization of this majorizer via a more easily separable preconditioned variant of ADMM (ordinary ADMM was used in [44]).

This paper is organized as follows. Section II presents a robust cost function for the phase retrieval problem. Section III introduces a convex majorizer for this optimization problem, and Section IV describes the use of ADMM to solve this convex subproblem. This section also introduces an optional regularization parameter normalization factor for Monte Carlo simulations and an existing adaptive heuristic for the ADMM penalty parameter [45] to greatly reduce manual tuning of these parameters. Experiments in Section V validate the parameter selection approach, compare convergence against a conventional algorithm applied to the robust phase retrieval problem, and evaluate the proposed method against existing

Manuscript received July 30, 2015; revised October 19, 2015; accepted October 21, 2015. Date of publication November 05, 2015; date of current version December 08, 2015. The work of D. S. Weller was supported by National Institutes of Health (NIH) Grant F32 EB015914. The work J.A. Fessler was supported by NIH Grant U01 EB018753, and an equipment donation from Intel. The work of Y. C. Eldar was supported by Israel Science Foundation Grant 170/10, SRC, and Intel Collaborative Research Institute for Computational Intelligence. The associate editor coordinating the review of this manuscript and approving it for publication was Prof. Jong Chul Ye.

D. S. Weller is with the Charles L. Brown Department of Electrical and Computer Engineering, University of Virginia, Charlottesville, VA 22904 USA (e-mail: dweller@virginia.edu).

A. Pnueli was with the Department of Electrical Engineering, Technion, Israel Institute of Technology, Haifa 32000, Israel (e-mail: ayelet.pnueli@gmail.com).

G. Divon, O. Radzyner, and Y. C. Eldar are with the Department of Electrical Engineering, Technion, Israel Institute of Technology, Haifa 32000, Israel (e-mail: giladd44@gmail.com; radzy@campus.technion.ac.il; yonina@ee.technion.ac.il).

J. A. Fessler is with the Department of Electrical Engineering and Computer Science, University of Michigan, Ann Arbor, MI 48109 USA (e-mail: fessler@umich.edu).

Color versions of one or more of the figures in this paper are available online at http://ieeexplore.ieee.org.

Digital Object Identifier 10.1109/TCI.2015.2498402

sparsity-promoting phase retrieval methods, including a 1-norm variant of sparse Fienup [31], the message-passing method PR-GAMP [30], and GESPAR [43]. Supplementary material includes a comparison with CPRL matrix lifting [37]; however, extreme memory requirements prevented CPRL from inclusion in the experiments with larger signals. Both 1D Monte Carlo and 2D simulations demonstrate that the proposed approach improves reconstruction quality versus all four competing methods when measurements contain both outliers and additive noise. Section VI discusses the proposed framework and algorithm and future extensions.

Code is online at http://people.virginia.edu/~dsw8c/sw.html. A supplement with additional experiments and derivations is available from IEEE Xplore.

II. Problem Statement

The following forward model describes the acquisition of M squared-magnitude measurements $\boldsymbol{y} = [y_1, \dots, y_M]^T$ from a general $M \times N$ linear transform $\boldsymbol{A}$ of a length-N (complex-valued) signal $\boldsymbol{x}$:

$$y_m = |[\boldsymbol{A}\boldsymbol{x}]_m|^2 + \nu_m, \quad m = 1, \dots, M, \tag{1}$$

where $[\boldsymbol{A}\boldsymbol{x}]_m = \sum_{n=1}^{N} A_{mn} x_n$, and $[\nu_1, \dots, \nu_M]^T$ is a vector of white Gaussian noise added to the squared-magnitude data. In contrast to adding noise to the complex $\boldsymbol{A}\boldsymbol{x}$ before taking the magnitude, as in [17], [30], this paper uses the post-magnitude noise model found in [25], [33], [35], [37], [43]. The vector $\boldsymbol{x}$ may represent either a 1D signal or a higher dimensional image, columnized.

Expanding beyond the conventional model in (1), the proposed framework aims to minimize the sum of negative log-likelihood functions $\sum_{m=1}^{M} -\ell(y_m; |[\boldsymbol{A}\boldsymbol{x}]_m|^q)$, for $q \geq 1$. The system may measure the magnitude $|[\boldsymbol{A}\boldsymbol{x}]_m|$ ($q = 1$), its square ($q = 2$), or a more general power ($q \geq 1$). More importantly, the data fit term extends more broadly to negative log-likelihood functions of the form $f(h([\boldsymbol{A}\boldsymbol{x}]_m; y_m))$, where $f(\cdot)$ is convex and nondecreasing (on $\mathbb{R}_+$), and the function

$$h(t; y) \triangleq |y - |t|^q| \tag{2}$$

of $t \in \mathbb{C}$ is the data fit error for fixed $y \in \mathbb{R}$. For this class of log-likelihood functions, the majorizer derived in Section III is convex in $\boldsymbol{x}$. To account for outliers in squared-magnitude measurements, this paper explores using the negative log-likelihood of a Laplace distribution:

$$-\ell\left(y_m; |[\boldsymbol{A}\boldsymbol{x}]_m|^2\right) \propto |y_m - |[\boldsymbol{A}\boldsymbol{x}]_m|^2|. \tag{3}$$

This data fit term takes the form of a 1-norm and has a long history of providing robustness to outliers, even if the measurement noise does not follow a Laplace distribution [46].

In this work, the 1-norm $\|\boldsymbol{x}\|_1$ regularizes the ill-posed phase retrieval problem, promoting image sparsity. Including a synthesis transform in the sensing matrix $\boldsymbol{A}$ directly extends this prior to synthesis-form sparsity. The proposed phase retrieval approach seeks a minimizer $\hat{\boldsymbol{x}} \in \mathbb{C}^N$ of

$$\arg\min_{\boldsymbol{x} \in \mathbb{C}^N} \Psi(\boldsymbol{x}) \triangleq \sum_{m=1}^{M} f(h([\boldsymbol{A}\boldsymbol{x}]_m; y_m)) + \beta \|\boldsymbol{x}\|_1, \tag{4}$$

where $\beta > 0$ is the regularization penalty parameter, and $h(\cdot; y_m)$ is given by (2). The reconstructed signal $\hat{\boldsymbol{x}}$ should be approximately sparse and roughly consistent with the data.

The proposed formulation in (4) shares a 1-norm data fit term with recent matrix lifting phase retrieval methods [40], [41], but with greatly reduced memory requirements. Many other existing approaches implicitly (via projections) or explicitly minimize the quadratic negative log-likelihood representing a Gaussian distribution and are not designed to accommodate this data fit term, limiting their robustness to outliers. The competing GESPAR method [43] also is restricted to 0-"norm" sparsity (counts the number of nonzeros).

III. Majorization of the Measurement Objective

The inverse problem formulation of phase retrieval is particularly difficult to solve because having only magnitude information makes the data fit term in the objective function $\Psi(\boldsymbol{x})$ in (4) nonconvex. Although conventional methods like nonlinear conjugate gradients (NLCG) [47] can approximately minimize $\Psi(\boldsymbol{x})$, the more sophisticated approach proposed in this section facilitates much more rapid convergence. This approach begins by constructing a convex majorizer for $\Psi(\boldsymbol{x})$. Section IV describes an iterative method for minimizing this majorizer effectively.

A. Derivation of the Majorizer

A majorizer $\phi(t; s; y)$ of the function $h(t; y)$ of t in (2) satisfies two properties: $\phi(s; s; y) = h(s; y)$, and $\phi(t; s; y) \geq h(t; y)$, for all t. Decreasing the majorizer value also reduces the value of the original function [48], so $h(t; y) < h(s; y)$ if t satisfies $\phi(t; s; y) < \phi(s; s; y)$. Assuming $f(\cdot)$ is convex and nondecreasing, and the majorizer $\phi(t; s; y)$ is convex in its argument t, $f(\phi(t; s; y))$ is also convex in t and majorizes $f(h(t; y))$ [49]. The approach below for finding $\phi(t; s; y)$ is related to the concave-convex procedure [50], [51].

Let $h_+(t; y) = |t|^q - y$, and $h_-(t; y) = y - |t|^q$ be functions of t. Then, $h(t; y) = \max\{h_+(t; y), h_-(t; y)\}$. As $q \geq 1$, $h_+(t; y)$ is already convex in t, but $h_-(t; y)$ is concave in t. When $y \leq 0$, $h(t; y) = h_+(t; y)$. Otherwise, a majorizer $\phi_-(t; s, y)$, convex in t, replaces $h_-(t; y)$. In this case, $\phi(t; s; y) \triangleq \max\{h_+(t; y),\ \phi_-(t; s, y)\}$ is convex in t and majorizes $h(t; y)$.

Since $h_-(t; y)$ is concave in t, its tangent plane about some point $s \in \mathbb{C}$ is a suitable convex majorizer:

$$\begin{aligned} \phi_-(t; s, y) &= (y - |s|^q) + (-q|s|^{q-1})\mathcal{R}\mathrm{e}\{e^{-\imath \angle s}(t - s)\} \\ &= y + (q - 1)|s|^q - q|s|^{q-1}\mathcal{R}\mathrm{e}\{te^{-\imath \angle s}\}. \end{aligned} \tag{5}$$

When $|s|^q < y$, $\phi_-(t; s, y)$ is tight among convex majorizers. However, when $|s|^q > y$, s is in the convex region of $h(\cdot; y)$, and the tangent plane for $\bar{s} \triangleq y^{1/q} e^{\imath \angle s}$ majorizes $h_-(t; y)$ more tightly in the range of $|t|^q \leq y$.

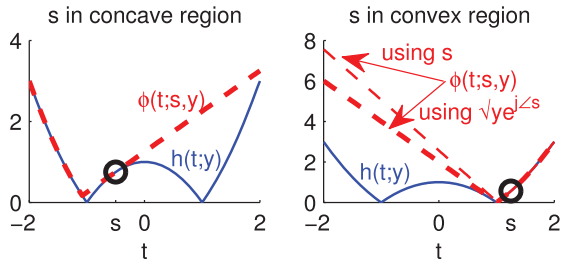

Fig. 1. The data fit error $h(t;y)$ (blue solid line) and the convex majorizer $\phi(t;s;y)$ (red dashed line) are plotted for real t, $y=1$, and $q=2$. Circles highlight the majorization points s for both examples. In the left figure, s is in the concave region of $h(\cdot;y)$, so the tangent plane at s is used in this region. In the right figure, s is located in the convex region of $h(\cdot;y)$, and the tangent plane at $y^{1/q}e^{\imath\angle s}$ is used instead.

In summary, the majorizer for the function $h(t;y)$ of t is

$$\phi(t;s;y)=\begin{cases} h_+(t;y), & y\le 0,\\ \max\{h_+(t;y),\ \phi_-(t;s,y)\}, & |s|^q<y,\\ \max\{h_+(t;y),\ \phi_-(t;\bar{s},y)\}, & 0<y\le|s|^q. \end{cases} \tag{6}$$

In the first case, $h(t;y)$ is already convex in t. The second and third cases correspond to s being in the concave and convex regions of $h(\cdot;y)$, respectively. Figure 1 portrays examples of the function $h(t;y)$ and its surrogate $\phi(t;s;y)$ in both the second (s in concave region) and third (s in convex region) cases. Substituting $\phi(t;s;y)$ for $h(t;y)$ in the objective $\Psi(\boldsymbol{x})$ in (4) yields its majorizer $\Phi(\boldsymbol{x};\boldsymbol{s})$, convex in $\boldsymbol{x}$:

$$\Phi(\boldsymbol{x};\boldsymbol{s})=\sum_{m=1}^{M} f(\phi([\boldsymbol{A}\boldsymbol{x}]_m;s_m;y_m))+\beta\|\boldsymbol{x}\|_1. \tag{7}$$

Having constructed $\Phi(\boldsymbol{x};\boldsymbol{s})$, the sequel describes how to minimize $\Psi(\boldsymbol{x})$ using this function.

B. Majorize–Minimize (MM) Algorithm

The proposed approach to solving (4) uses the majorize-minimize (MM) scheme [48], [52] outlined in Algorithm 1. Each iteration of this MM method decreases $\Psi(\boldsymbol{x})$ by minimizing $\Phi(\boldsymbol{x};\boldsymbol{s})$ over $\boldsymbol{x}$, converging to a critical point of $\Psi(\boldsymbol{x})$ when $\Psi(\cdot)$ and $\Phi(\cdot;\boldsymbol{s})$ are differentiable at every non-critical majorization point $\boldsymbol{x}=\boldsymbol{s}$. Running the algorithm for multiple different initial choices of $\boldsymbol{s}^0$ increases the chance of finding a global optimum of the original nonconvex problem. Many phase retrieval methods also employ multiple initializations, as do nonconvex solvers more generally.

Algorithm 1. Majorize-minimize Scheme for Solving (4).

Require: I_{mm}, ϵ_{mm}, random $\boldsymbol{s}^0\in\mathbb{C}^M$.
for $i=1:I_{\text{mm}}$ **do**

$$\boldsymbol{x}^i\leftarrow\arg\min_{\boldsymbol{x}}\Phi(\boldsymbol{x};\boldsymbol{s}^{i-1}). \tag{8}$$

$$\boldsymbol{s}^i\leftarrow\boldsymbol{A}\boldsymbol{x}^i. \tag{9}$$

if $\|\boldsymbol{s}^i-\boldsymbol{s}^{i-1}\|<\epsilon_{\text{mm}}$ **then break**
end if
end for

IV. Solving the Majorized Objective With ADMM

Jointly minimizing M pairwise maximum functions to minimize (7) directly would be combinatorially hard. Instead, introducing an auxiliary vector $\boldsymbol{u}=\boldsymbol{A}\boldsymbol{x}$, each function in the summation in (7) depends only on a single $u_m=[\boldsymbol{u}]_m$. The constrained problem using this auxiliary variable is

$$\{\boldsymbol{x}^{i+1},\boldsymbol{u}\}\leftarrow\arg\min_{\boldsymbol{x},\boldsymbol{u}}\sum_{m=1}^{M} f(\phi(u_m;s_m;y_m))+\beta\|\boldsymbol{x}\|_1,\quad \text{s.t. } u_m=[\boldsymbol{A}\boldsymbol{x}]_m,\quad m=1,\dots,M. \tag{10}$$

The alternating direction method of multipliers (ADMM) framework [45], [53]–[55] uses the augmented Lagrangian of this constrained problem:

$$\mathcal{L}_A(\boldsymbol{x},\boldsymbol{u};\boldsymbol{b})\triangleq\sum_{m=1}^{M} f(\phi(u_m;s_m;y_m))+\beta\|\boldsymbol{x}\|_1+\frac{\mu}{2}\|\boldsymbol{A}\boldsymbol{x}-\boldsymbol{u}+\boldsymbol{b}\|_2^2, \tag{11}$$

where $\boldsymbol{b}\in\mathbb{C}^M$ and $\mu>0$ are the scaled dual vector (Lagrange multipliers) and augmented Lagrangian penalty parameter, respectively. The implementation of ADMM in Algorithm 2 minimizes (11), subject to $\boldsymbol{u}=\boldsymbol{A}\boldsymbol{x}$. To simplify notation here and in subsequent sections, define $d_m=[\boldsymbol{A}\boldsymbol{x}+\boldsymbol{b}]_m$. Initially, $\boldsymbol{x}^0$, $\boldsymbol{u}^0$, and $\boldsymbol{b}^0$ are set to $\boldsymbol{0}$. In later iterations, the last $\boldsymbol{x}$, $\boldsymbol{u}$, and $\boldsymbol{b}$ from the previous run of ADMM "warm-start" the next run. Methods for updating $\boldsymbol{x}$ and $\boldsymbol{u}$ depend on the specific $\boldsymbol{A}$ and $f(\cdot)$ used. This paper provides details for general $\boldsymbol{A}$ with the 1-norm data fit term.

Algorithm 2. ADMM method for solving (11).

Require: I_{ADMM}, ϵ_{ADMM}, $\boldsymbol{x}^0$, $\boldsymbol{u}^0$, $\boldsymbol{b}^0$, $\boldsymbol{y}$, β, μ.
for $i=1:I_{\text{ADMM}}$ **do**

$$\boldsymbol{x}^i\leftarrow\arg\min_{\boldsymbol{x}}\beta\|\boldsymbol{x}\|_1+\frac{\mu}{2}\left\|\boldsymbol{A}\boldsymbol{x}-(\boldsymbol{u}^{i-1}-\boldsymbol{b}^{i-1})\right\|_2^2. \tag{12}$$

for $m=1:M$ **do**
$d_m\leftarrow[\boldsymbol{A}\boldsymbol{x}^i+\boldsymbol{b}^{i-1}]_m$.

$$u_m^i\leftarrow\arg\min_{u} f(\phi(u;s_m;y_m))+\frac{\mu}{2}|u-d_m|^2. \tag{13}$$

end for

$$\boldsymbol{b}^i\leftarrow\boldsymbol{b}^{i-1}+\boldsymbol{A}\boldsymbol{x}^i-\boldsymbol{u}^i. \tag{14}$$

if $\|\boldsymbol{x}^i-\boldsymbol{x}^{i-1}\|<\epsilon_{\text{ADMM}}$ **then break**
end if
end for

A. Updating x

The update for $\boldsymbol{x}$ in the preceding ADMM framework has the extensively studied synthesis form of compressed sensing (CS) [56]–[59]. Various CS algorithms may be appropriate, depending on the structure of $\boldsymbol{A}$.

If $\boldsymbol{A}$ is left-unitary, so that $\boldsymbol{A}'\boldsymbol{A} = \boldsymbol{I}$, then the least-squares term in (12) simplifies to $\|\boldsymbol{x} - \boldsymbol{A}'(\boldsymbol{u}^i - \boldsymbol{b}^i)\|_2^2$, plus a constant term. In this case, updating $\boldsymbol{x}$ becomes soft thresholding: $\boldsymbol{x}_n^{i+1} \leftarrow \mathrm{soft}([\boldsymbol{A}'(\boldsymbol{u}^i - \boldsymbol{b}^i)]_n; \frac{\beta}{\mu})$, where

$$\mathrm{soft}(x;\tau) = \frac{x}{|x|}\max\{|x| - \tau, 0\}. \tag{15}$$

Otherwise, an iterative algorithm like FISTA [60] could be embedded within the ADMM method [44]. Instead, we use "preconditioned" ADMM (PADMM) [61], [62] accelerated[1] using Nesterov momentum [64], essentially using a single FISTA step as the $\boldsymbol{x}$-update in (12):

$$\boldsymbol{x}^i \leftarrow \mathrm{soft}\left(\boldsymbol{z}^{i-1} - \frac{1}{c}\boldsymbol{A}'(\boldsymbol{A}\boldsymbol{z}^{i-1} - \boldsymbol{u}^{i-1} + \boldsymbol{b}^{i-1}); \frac{\beta}{\mu c}\right). \tag{16}$$

$$t^i \leftarrow \left(1 + \sqrt{1 + 4(t^{i-1})^2}\right)/2. \tag{17}$$

$$\boldsymbol{z}^i \leftarrow \boldsymbol{x}^i + \frac{t^{i-1} - 1}{t^i}\left(\boldsymbol{x}^i - \boldsymbol{x}^{i-1}\right). \tag{18}$$

The scalar c must satisfy $c\boldsymbol{I} \succeq \boldsymbol{A}'\boldsymbol{A}$; it can be precomputed using power iterations, or found directly in many cases. For example, $c = 1$ for the undersampled unitary discrete Fourier transform (DFT) used in the experiments in this paper. "Gradient"-based adaptive restarting [65] can help avoid divergence: when the momentum term $\boldsymbol{x}^i - \boldsymbol{x}^{i-1}$ points away from $\boldsymbol{x}^i - \boldsymbol{z}^{i-1}$, the momentum is reset ($t^{i-1} = 0, t^i = 1$). While PADMM does not possess the same convergence guarantees as regular ADMM, faster convergence may be possible by adjusting the dual update in (14); see [66].

B. Updating u

Because of the proposed variable-splitting, updating the auxiliary vector $\boldsymbol{u}$ can be performed element-by-element. Since $f(\cdot)$ is monotone nondecreasing, and $\phi(u_m; s_m; y_m)$ is the pointwise maximum of two functions (for $y_m > 0$), $f(\phi(u_m; s_m; y_m)) = \max\{f_+(u_m),\ f_-(u_m)\}$, where

$$f_+(u_m) \triangleq \frac{\mu}{2}|u_m - d_m|^2 + f(h_+(u_m; y_m)), \tag{19}$$

$$f_-(u_m) \triangleq \frac{\mu}{2}|u_m - d_m|^2 + \begin{cases} 0, & y_m \le 0, \\ f(\phi_-(u_m; s_m, y_m)), & |s_m|^q < y_m, \\ f(\phi_-(u_m; \bar{s}_m, y_m)), & 0 < y_m \le |s_m|^q, \end{cases} \tag{20}$$

and $d_m = [\boldsymbol{A}\boldsymbol{x} + \boldsymbol{b}]_m$. Updating u_m is equivalent to solving

$$\arg\min_{u,T}\ T,\ \text{s.t. } f_+(u) \le T, f_-(u) \le T. \tag{21}$$

The minimizing T corresponds to the value of $f(\phi(u; s_m; y_m))$ at its minimum (with respect to u). The Lagrangian of (21) is $T + \gamma_+(f_+(u) - T) + \gamma_-(f_-(u) - T)$, with Lagrange multipliers $\gamma_+, \gamma_- \ge 0$. Differentiating yields $\gamma_+ + \gamma_- = 1$. Three possibilities exist:

1) $\gamma_+ = 1$, $\gamma_- = 0$: The optimal $u = u_+$ minimizes $f_+(u)$ and satisfies $f_+(u_+) > f_-(u_+)$.
2) $\gamma_+ = 0$, $\gamma_- = 1$: The optimal $u = u_-$ minimizes $f_-(u)$ and satisfies $f_-(u_-) > f_+(u_-)$.
3) $\gamma_+, \gamma_- > 0$: Both $f_+(u)$ and $f_-(u)$ equal T. The optimal $u = u_\pm$ minimizes both of these functions along the curve $f_+(u) = f_-(u)$.

For $f(\cdot)$ corresponding to the 1-norm data fit term in (3) on squared-magnitude measurements ($q = 2$), the optimal values of u for each case for the mth measurement are

$$u_+ = \frac{\mu}{2 + \mu}d_m, \tag{22}$$

$$u_- = \frac{2s_m}{\mu} + d_m, \text{ and} \tag{23}$$

$$u_\pm = \sqrt{2(y_m + |s_m|^2)}e^{\imath\angle((2+\mu)s_m + \mu d_m)} - s_m. \tag{24}$$

When $|s_m|^q \ge y$, we replace s_m above with $\bar{s}_m$. The functions $f_+(u)$ and $f_-(u)$ are evaluated for each case to determine which of the three cases applies. These expressions, and corresponding expressions for quadratic $f(\cdot)$, are derived in the supplement.

C. Computational Complexity

The proposed algorithm consists of nested layers of iterative methods, adding complexity compared to simpler methods like nonlinear conjugate gradients (NLCG). Multiple initial values of $\boldsymbol{s}^0$ are tested to increase the likelihood of finding a global minimum. For each initial value, several iterations of the MM algorithm in Algorithm 1 are run. Finally, for each outer iteration of the MM method, several inner iterations of ADMM (or PADMM) are performed.

Each iteration of ADMM/PADMM involves updating $\boldsymbol{x}$, $\boldsymbol{u}$, and $\boldsymbol{b}$. Updating $\boldsymbol{x}$ involves two matrix-vector products with $\boldsymbol{A}$ or $\boldsymbol{A}'$. Reusing the calculated value of $\boldsymbol{A}\boldsymbol{x}$ avoids recomputing it through the remainder of the iteration. When $\boldsymbol{A}$ is a DFT matrix, the cost is roughly $O(N \log N)$ for each. At least for the 1-norm data fit term with squared-magnitude measurements, each candidate u_m is a simple function of d_m, s_m, and y_m, so that the cost of updating $\boldsymbol{u}$ is roughly $O(M)$. Updating $\boldsymbol{b}$ is a simple addition, again scaling as $O(M)$. The overall cost of an ADMM iteration is $O(N \log N + M)$.

Without acceleration, the error in $\boldsymbol{x}$ converges roughly as $O(1/I_{\mathrm{ADMM}})$ for preconditioned ADMM (I_{ADMM} is the number of iterations) [61]. Empirical convergence behavior of our ADMM implementation is established in the automatic ADMM parameter tuning experiment in Section V-B. Computational costs are reported along with the simulations in Section V.

[1]This method differs from accelerated ADMM [63] that applies momentum without introducing the separable majorizer simplifying the quadratic augmented Lagrangian penalty in (11) we depend on here.

When transitioning from relatively small 1D experiments to a much larger 2D experiment, the number of MM iterations (I_{mm}) only increases modestly, and the number of PADMM iterations and initializations remains constant.

D. Parameter Selection

The regularization parameter β controls the level of sparsity in the reconstructed signal. Additionally, the ADMM penalty parameter μ impacts the convergence rate of the inner ADMM/PADMM algorithm. Introducing an adaptive heuristic for μ and a normalization factor for β avoids manual tuning of these parameters for every experiment.

For ADMM penalty parameter μ, the automatic heuristic in [45] and quadratic-optimal strategy in [67] provide alternatives to adjusting μ manually. The chosen adaptive method, described in [45], starts at some initial value and adapts μ every 10 ADMM iterations by comparing the residual $\boldsymbol{u}^i - \boldsymbol{A}\boldsymbol{x}^i$ and dual residual $\mu\boldsymbol{A}'(\boldsymbol{u}^i - \boldsymbol{u}^{i-1})$. This method is compared against using fixed (manually tuned) μ in Section V-B.

The choice of regularization parameter β, which reflects prior knowledge about the sparsity of the desired signal, also greatly influences the reconstruction. All the competing methods investigated in this paper use this type of parameter, or the related sparsity factor K. While K may be more-or-less known, learning β from K is not straightforward [59]. In the Monte Carlo simulations that follow, the optimum value of β varies based on the true 1-norm of $\boldsymbol{x}$ and the actual data discrepancy. Not knowing these a priori, this algorithm uses a simple normalization framework for β that requires only the measurements $\boldsymbol{y}$ and the approximate noise level/number of outliers. Differentiating $\sum_m f(h([\boldsymbol{A}\boldsymbol{x}]_m; y_m))$ with respect to $\boldsymbol{x}$, obtains (for a 1-norm data fit term with $q = 2$)

$$2\boldsymbol{A}'\boldsymbol{D}_{\text{noise}}\boldsymbol{A}\boldsymbol{x}, \tag{25}$$

where $\boldsymbol{D}_{\text{noise}}$ is a diagonal matrix with entries $[\boldsymbol{D}_{\text{noise}}]_{m,m} = \text{sign}(|[\boldsymbol{A}\boldsymbol{x}]_m|^2 - y_m)$. To make this expression as consistent as possible as the noise level or number of measurements changes, the data fit term is normalized according to the 2-norm of (25). When $\boldsymbol{A}$ is an undersampled (unitary) DFT, the 2-norm becomes

$$\left(\sum_{m:|[\boldsymbol{A}\boldsymbol{x}]_m|^2 \neq y_m} |[\boldsymbol{A}\boldsymbol{x}]_m|^2\right)^{1/2}.$$

Assuming zero-mean noise, the expected value of $|[\boldsymbol{A}\boldsymbol{x}]_m|^2$ is y_m. When y_m is an outlier, this is not the case, and $|[\boldsymbol{A}\boldsymbol{x}]_m|^2$ is approximated by the average value of the measurements not likely to be outliers. Assuming the M_{out} largest measurements are the most likely outliers, and $\bar{y}$ represents the arithmetic mean of the remaining measurements, the normalizer becomes

$$\left(M_{\text{out}}\bar{y} + \sum_{m:\text{y}_m \text{not outlier}} y_m\right)^{1/2} = (M_{\text{out}}\bar{y} + (M - M_{\text{out}})\bar{y})^{1/2} = (M\bar{y})^{1/2}. \tag{26}$$

With this normalization, the proposed algorithm can be applied to a whole set of signals without manually tuning β for each one. Although outliers are unknown a priori, the estimation error of $\bar{y}$ should be small when $M_{\text{out}} \ll M$.

TABLE I
COMPARISON OF RECONSTRUCTION METHODS

Method	Implementation	Sparsity	Data Fit Term
L_1-Fienup [31]	alternating projections	1-norm	quadratic (projection)
GESPAR [43]	greedy	0-"norm"	quadratic
PR-GAMP [30]	message-passing	0-"norm"	quadratic[2]
Proposed	MM, (P)ADMM	1-norm	1-norm (ℓ_1)

TABLE II
RECONSTRUCTION METHOD PARAMETERS

All methods	$q = 2$, 50 Monte Carlo trials, ≥ 50 inits each
L_1-Fienup	50 iters/init, 5 conjugate gradient iterations for data projection (2D recon only), 10^{-4} stop tol
GESPAR	100 Gauss-Newton iters per GESPAR step, 10^{-5} stop tol, random measurement weights on
PR-GAMP	20 expectation-maximization iters, 200 inner iters each, 10^{-4} stop tol
Proposed	$\mu = 1$ start, $I_{\text{ADMM}} = 100$ (PADMM for $M < N$), adapt μ every 10 iters, $I_{\text{mm}} = 10$, 10^{-10} stop tol

V. EXPERIMENTAL SETUP AND RESULTS

Simulations throughout this paper consist of generating a length-N sparse signal with K nonzero coefficients, acquiring M samples of the squared-magnitude DFT of that signal, reconstructing the signal using the proposed and/or competing algorithms listed in Table I, and comparing the reconstructed signals against the true signal.

A. Experimental Setup

This section describes the general setup common to all experiments. These experiments are simulations, generating the sparse support of each true signal at random, and randomly sampling the amplitude and phase of each nonzero coefficient uniformly between 0 and 1 (amplitude) and 0 and 2π (phase).

For each simulated signal, M noise-free measurements are randomly selected from the squared-magnitude of the signal's DFT coefficients. Randomly selected outliers are set to have an amplitude between one and two times the maximum measurement. Additionally, Gaussian or Laplace noise (40 dB SNR unless stated otherwise) are added to all the measurements.

The reconstructions are performed using multiple initializations, and the "best" reconstructed signal for each method is retained. For the proposed method, 50 initializations are performed per trial, 100 for the fully-sampled ($M = N$) case, and the lowest value of $\Psi(\boldsymbol{x})$ determines the best reconstruction. The regularization parameter β is held fixed for the Monte Carlo experiments; the ADMM penalty parameter μ is automatically adapted [45], not manually tuned. Other reconstruction parameters are provided in Table II. Competing methods include the GESPAR greedy method [43], the L_1-Fienup method (sparse Fienup [31] with the image-domain projection

[2]The PR-GAMP method is implemented for noise applied before taking the (squared)-magnitude, unlike the others here that assume noise is added to the (squared)-magnitude measurements.

modified to project the signal onto the ℓ_1-ball with radius β_{sf}, like [29]), and the message passing algorithm PR-GAMP [30]. These other methods are run for at least 50 initializations, but often more to allow for the same total amount of computation (measured via tracking the number of multiplies by $\boldsymbol{A}$ or $\boldsymbol{A}'$). The best reconstructions are chosen for L_1-Fienup, GESPAR, and PR-GAMP according to the smallest 2-norm data discrepancy. In the supplement, the proposed method is compared with compressive matrix lifting (CPRL) [37]. As CPRL requires significantly more memory to run, with a length-128 complex signal requiring upwards of 17 GB of memory, the experiment featuring CPRL uses a much smaller signal ($N = 64$).

Sparsity and Fourier coefficient magnitudes are invariant to spatial shifts, reversal, and global phase. Thus, the error computation is relative to the best alignment/reversal and global phase for each reconstructed signal. The best alignment is identified for both the reconstructed signal and its reversed version by cross-correlation with the true signal. A global phase term is then estimated from the version with the best alignment. Reconstruction errors are reported relative to the true signal using the median of the squared errors (normalized by N) over the set of trials. This peak-signal-to-error ratio (PSER) is converted to dB scale:

$$\text{PSER} = -10\log_{10}(\text{median squared error}), \tag{27}$$

where the maximum true signal amplitude is one.

B. Validating Parameter Selection Methods

The first experiment compares convergence of the majorizer objective value in (7) for automatically adapted μ and fixed, manually tuned μ. Simulations of a 1D signal are repeated for both $K = 6$ and $K = 8$ sparse coefficients, and both $M = 64$ (undersampled case, using PADMM) and $M = N = 128$ (fully-sampled case, using ADMM) squared-magnitude measurements, corrupted by both additive Gaussian noise (40 dB SNR) and 5 outliers. For each experiment, we run one set of ADMM/PADMM iterations with the 1-norm data fit distribution, some with a fixed penalty parameter μ (only the best are shown), and others with the adaptive method, starting from different initial values. For these experiments, the regularization parameter β is chosen to portray a range of convergence behaviors, not to optimize the reconstruction.

For sparsity $K = 6$ and both $M = 64$ and $M = N = 128$ noisy measurements, Figure 2 portrays the objective function convergence rates over $I_{\text{ADMM}} = 100$ ADMM/PADMM iterations for the three best fixed choices of μ, relative to the best overall objective function value observed after 400 iterations. These are compared against the adaptive method starting at the best ($\mu = 1$) and a suboptimal ($\mu = 0.1$) initial value. This experiment verifies that the adaptive method achieves nearly as good convergence as the best fixed method in both the undersampled (using PADMM) and fully-sampled (using ADMM) cases, even when not initialized to the best choice of μ. The same experiment for different sparsity $K = 8$ yields similar results to the example shown. Since the adaptive method appears to ensure rapid convergence across varying degrees

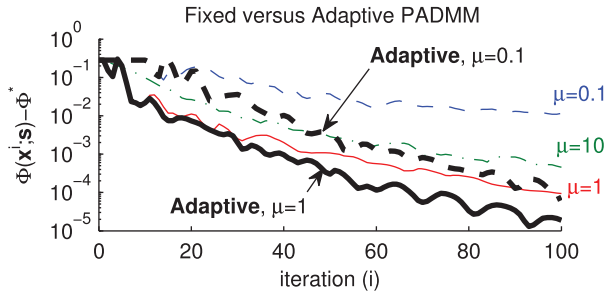

(a) PADMM convergence for $K = 6$, $M = 64$, $N = 128$.

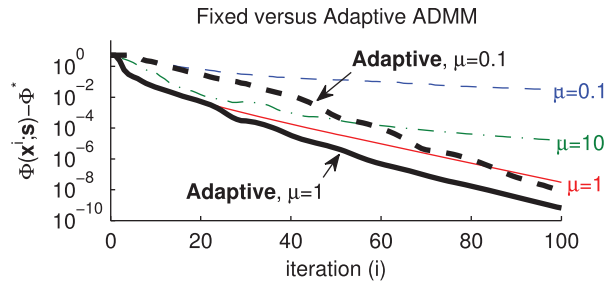

(b) PADMM convergence for $K = 6$, $M = N = 128$.

Fig. 2. The objective function $\Phi(\boldsymbol{x}^i; \boldsymbol{s})$, relative to converged value Φ^*, is plotted versus ADMM/PADMM iteration i for ADMM/PADMM using fixed (thin, color lines) and adaptive (thick, black lines) penalty parameters (μ).

of measurements and sparsities, this adaptive heuristic scheme with initial $\mu = 1$ is employed throughout the experiments that follow, without any additional tuning.

To observe how sensitive the regularization parameter β with the proposed normalization factor is as the sparsity level K or number of measurements M varies, the proposed algorithm is evaluated on sets of 50 simulated signals, each of whose squared-magnitude measurements are corrupted with additive Gaussian noise (40 dB SNR) and 5 outliers. In [44], β scales roughly linearly with the number of measurements for the proposed method without normalization. With normalization, the optimal β appears to remain fairly constant between 0.1 and $10^{-0.9}$. Figure 3 plots the median squared error (lines) and error quartiles (boxes) versus the regularization parameter β for (a) different sparsity levels $K = 3, 5, 6, 8$, holding $M = N = 128$ fixed, and for (b) different measurements $M = 32, 64, 96, 128$, holding $K = 3$ fixed. The β values found in this experiment are fixed and reused in all the Monte Carlo experiments, regardless of noise level or type, with no further tuning.

To ensure competing methods are not at a disadvantage, both GESPAR and PR-GAMP are provided the true sparsity (K) for each signal. For the L_1-Fienup method, the radius β_{sf} of the ℓ_1-ball constraint is set to the 1-norm of the true signal.

C. Rapid Convergence With Preconditioned ADMM

The robust phase retrieval problem described in (4) can be solved via conventional methods including nonlinear conjugate gradients (NLCG), if the 1-norm is approximated by a differentiable function. However, close approximations to the 1-norm have a high curvature that slow convergence of NLCG. We compared empirically the convergence rates of NLCG and

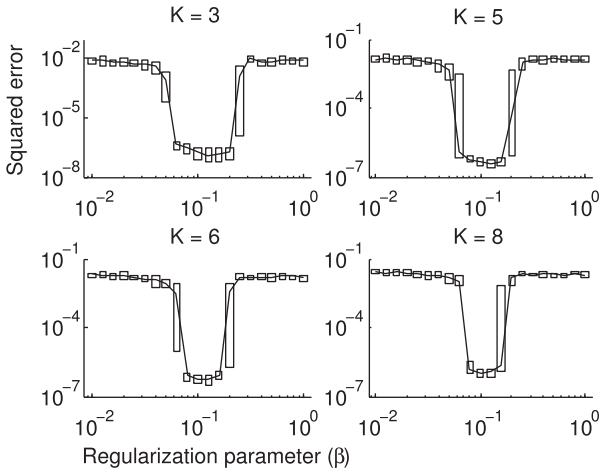

(a) Squared errors for $M = N = 128$ and $K = 3, 5, 6, 8$.

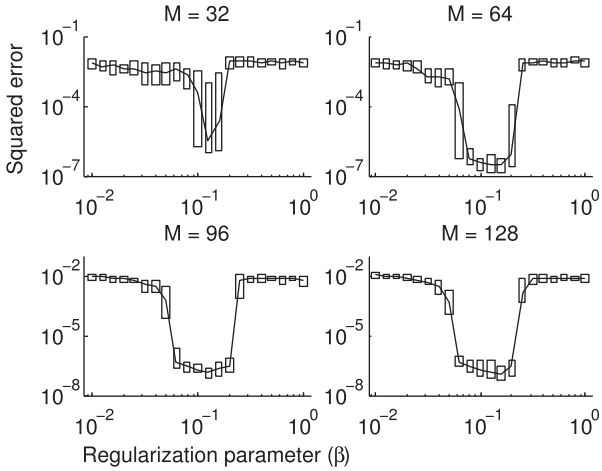

(b) Squared errors for $K = 3$ and $M = 32, 64, 96, 128$.

Fig. 3. The median (lines) and quartiles (boxes) of 50 trials reconstructed using the proposed method with a 1-norm data fit term are plotted versus regularization parameter β for varying (a) signal sparsity levels K, and (b) measurements M. The signal length $N = 128$.

the proposed algorithm. Representative length-128 signals, one with sparsity $K = 6$ and $M = 64$ noisy measurements, and the other with sparsity $K = 8$ and $M = 128$ noisy data (both 40 dB SNR Gaussian noise and 5 outliers), are reconstructed using both methods. First, the MM method with adaptive preconditioned ADMM is run for 50 initializations, and the best result (minimum objective value) is kept. Then, the NLCG method is run for that same best initializer, for a number of iterations equivalent to the total number of inner iterations of the preconditioned ADMM method. The objective function in (4) is plotted for each NLCG iteration (solid line) and every MM iteration (circles) in Fig. 4. The plotted objective functions converge at very different rates, with a distinct advantage to the proposed MM algorithm with adaptive preconditioned ADMM.

D. Monte Carlo Comparisons (1D)

This section compares the proposed phase retrieval method against the competing methods listed in Table I via 50-trial

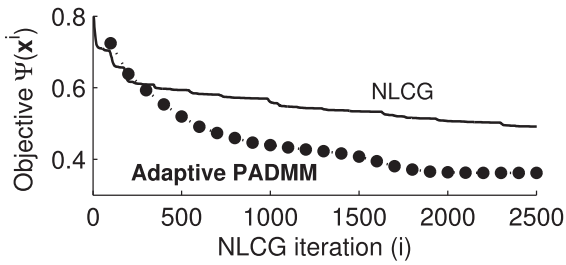

(a) Convergence for $K = 6$, $M = 64$, $N = 128$.

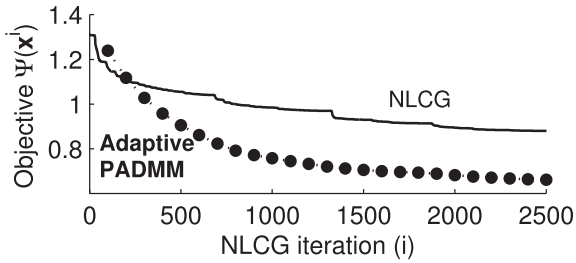

(b) Convergence for $K = 8$, $M = N = 128$.

Fig. 4. The objective function $\Psi(\boldsymbol{x}^i)$ in (4) is plotted versus NLCG iteration i and the equivalent MM iteration for both NLCG (solid line) and MM with adaptive preconditioned ADMM (circles), for K-sparse length-N signals from length-M noisy data (40 dB SNR AWGN noise, 5 outliers).

Monte Carlo simulations with different values of sparsity K, number of measurements M, and noise/outlier levels and types. All the comparisons in this section involve length-128 1D signals and measurements corrupted with both outliers and either Gaussian or Laplace noise. The same β values identified in Section V-B are reused here for all types of noise.

The first test evaluates the proposed algorithm on measurements corrupted by Gaussian noise (40 dB SNR) and 5 outliers. Fig. 5 depicts PSER values corresponding to median squared errors for the proposed and competing methods. Equivalent comparisons for measurements corrupted by Laplace noise (also 40 dB SNR) and 5 outliers are shown in Fig. 6. The median squared errors for the proposed method show significant improvement over competing methods in both cases. The supplement depicts the PSER values for the mean squared errors in both experiments. Regarding runtimes, as measured by the multiplications by $\boldsymbol{A}$ or $\boldsymbol{A}'$ (the dominant computations), the proposed method runs for the same number of iterations for all sparsities K and measurements M, except the number of initializations is doubled for $M = N$ for robustness (this is responsible for the upper limit on the range of multiplies for all the methods). Otherwise, the amount of computation remains nearly constant.

To see how the noise level or number of outliers affects reconstruction quality, Monte Carlo simulations are conducted for the Gaussian noise + outliers case, varying the number and variance of outliers and SNR of the additive noise. Figure 7 shows median PSER values for $K = 3$ sparse signals ($N = 128$), whose measurements are corrupted by 2, 4, 8, 16 outliers, with a range [1,2] times the maximum measurement value, holding the Gaussian noise SNR fixed at 40 dB. Supplementary material contains a similar figure for a smaller outlier range $[1, \sqrt{2}]$ and for $K = 5$ sparse signals. Fig. 8 depicts

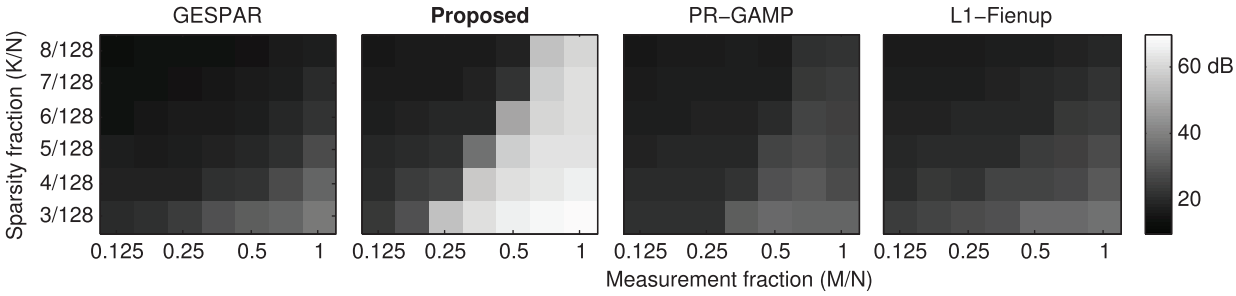

Fig. 5. The PSER of 50 trials reconstructed using GESPAR, the proposed method, PR-GAMP, and L_1-Fienup, for a range of measurement (M/N) and sparsity fractions (K/N), for measurements with 40 dB SNR Gaussian noise and 5 outliers. Computations (1000's of multiplies by $\boldsymbol{A}$, $\boldsymbol{A}'$): 110–1354 (GESPAR), 94–218 (proposed), 111–250 (PR-GAMP), 103–218 (L_1-Fienup).

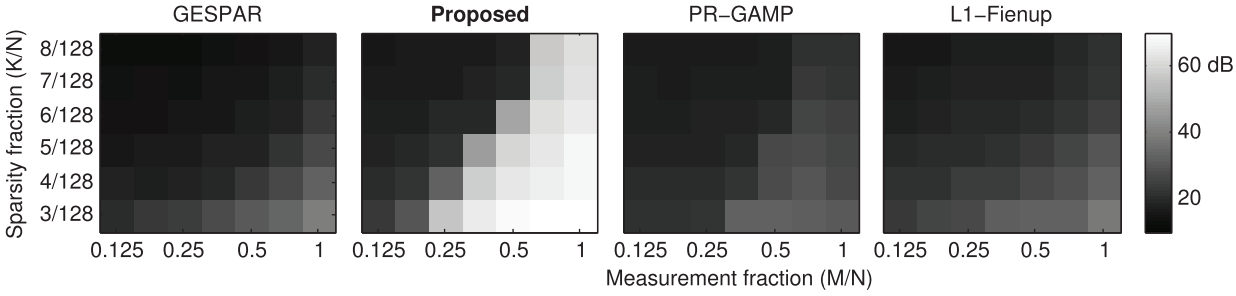

Fig. 6. The PSER of 50 trials reconstructed using GESPAR, the proposed method, PR-GAMP, and L_1-Fienup, for a range of measurement (M/N) and sparsity fractions (K/N), for measurements with 40 dB SNR Laplace noise and 5 outliers. Computations (1000's of multiplies by $\boldsymbol{A}$, $\boldsymbol{A}'$): 110–1361 (GESPAR), 94–218 (proposed), 110–294 (PR-GAMP), 103–218 (L_1-Fienup).

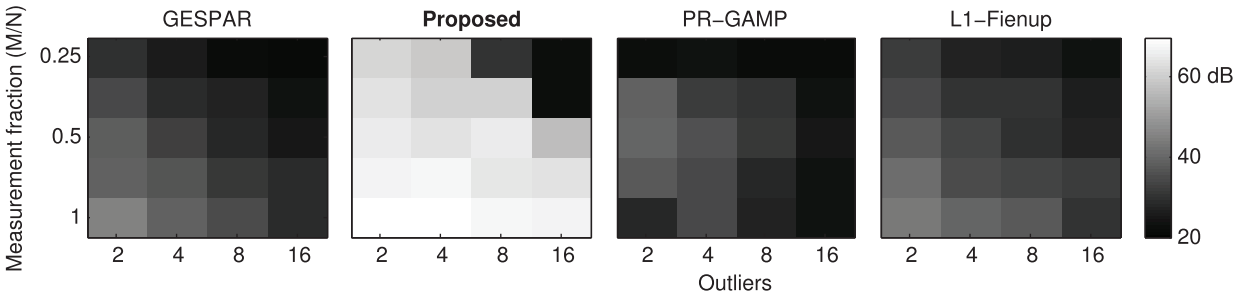

Fig. 7. The PSER of 50 trials reconstructed using GESPAR, the proposed method, PR-GAMP, and L_1-Fienup, for a range of measurement (M/N) and outliers, for $K = 3$ and measurements with 40 dB SNR Gaussian noise. Computations (1000's of multiplies by $\boldsymbol{A}$, $\boldsymbol{A}'$): 109–537 (GESPAR), 103–217 (proposed), 110–248 (PR-GAMP), 108–218 (L_1-Fienup).

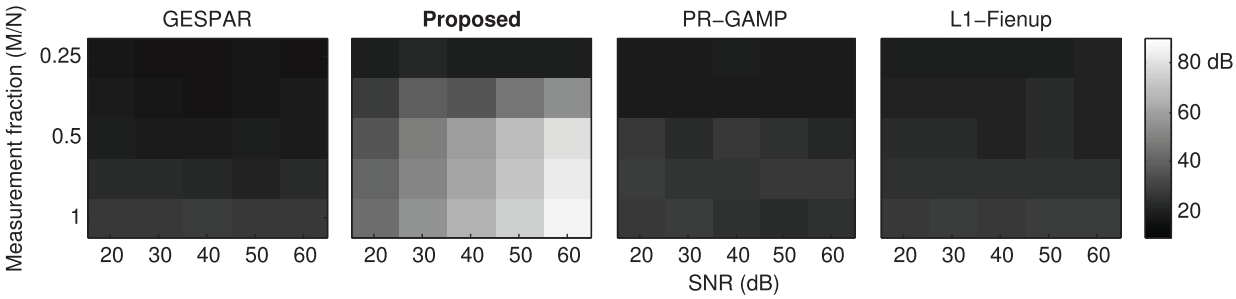

Fig. 8. The PSER of 50 trials reconstructed using GESPAR, the proposed method, PR-GAMP, and L_1-Fienup, for a range of measurement (M/N) and Gaussian noise SNRs, for $K = 5$ and measurements with 5 outliers. Computations (1000's of multiplies by $\boldsymbol{A}$, $\boldsymbol{A}'$): 106–497 (GESPAR), 94–215 (proposed), 107–266 (PR-GAMP), 106–218 (L_1-Fienup).

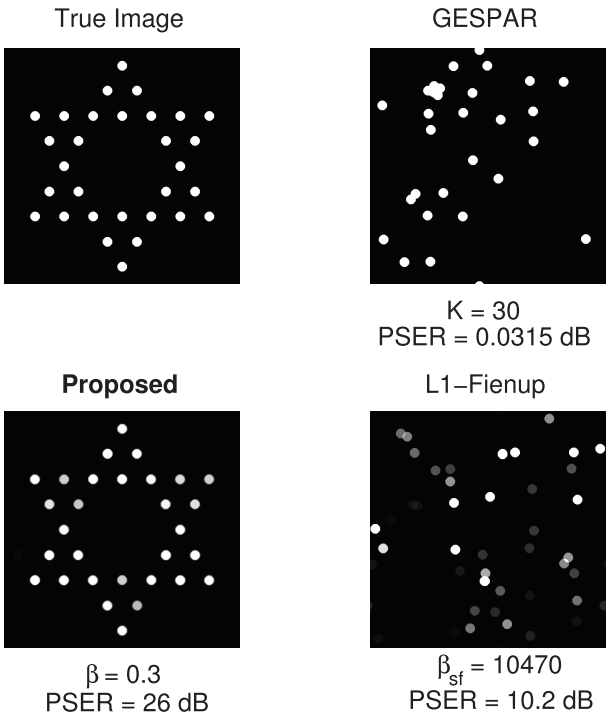

Fig. 9. The best reconstruction (with regularization parameter β) for the proposed method is compared against competing methods with the optimal (true) values of β_{sf} or K. These images are shown for the 512×512-pixel star of David phantom, from $M = N/2$ measurements, with 60 dB AWGN noise and 1% (1311) outliers. The PR-GAMP method (not shown) converged to a blank (all zero) image. Computations (1000's of multiplies): 584 (GESPAR), 218 (proposed), 218 (PR-GAMP), 218 (L_1-Fienup).

improvements for $K = 5$ sparse signals ($N = 128$) with measurements with 20, 30, 40, 50, 60 dB SNR Gaussian noise, holding the number and range of outliers fixed at 5 and [1,2], respectively. The supplement contains the corresponding plot for $K = 3$. The improvement in squared error appears significant over a wide range of noise levels and numbers of outliers.

E. Image Comparisons (2D)

This experiment examines image reconstruction with undersampled measurements corrupted by outliers and additive Gaussian noise. The $N = 512 \times 512$-pixel star of David phantom used in [44] is inspired by the real example image shown in [68]. The pattern in the image is constructed using 30 discs, each 21-pixels wide. A dictionary of these discs (at all 512×512 positions) is used as the synthesis transform for all the reconstructions. Since the dictionary is shift-invariant, implementing the dictionary via multiplication in frequency saves computation and storage for all the methods. The squared-magnitudes of the 2D DFT of this image are randomly undersampled by a factor of two ($M = N/2 = 131,072$). One percent of the measurements are changed to outliers, and 60 dB SNR additive Gaussian noise is added to all measurements. The phantom is reconstructed using both the proposed and competing algorithms, resulting in the images in Figure 9.

To conserve space, the blank image produced by the PR-GAMP method is not shown here. Reconstructions of the same image with fewer outliers are provided in the supplementary material. In terms of scalability, the proposed method works well without much adjustment; only the number of MM iterations I_{mm} changes (from 10 to 20), doubling the number of multiplies versus the proposed method in the 1D case. The ADMM penalty parameter remains the same (adaptive) as in the 1D experiments, but we reexamine the regularization parameters for all the methods. The true K and β_{sf} are fixed, while several values for β between 0.1 and 0.4 are tested to account for the smaller K/N of the 2D image. The advantage of the proposed method is clear, as none of the competing methods recovered the true image, even when running GESPAR, PR-GAMP, and L1-Fienup for at least as many initializations and at least as much (often, much more) computation as the proposed method. In the supplement, this improvement in quality is apparent even with extremely few outliers.

VI. Discussion

Undersampled phase retrieval relies heavily on side information to reproduce a quality image. Employing sparsity in the image domain, or dictionary-based sparsity, helps identify the best image among all those that share the same magnitude Fourier spectrum. Resolving this ambiguity becomes even more challenging in the face of measurement noise, especially outliers. The proposed method using a 1-norm data fit term excels at reconstructing images despite these conditions, greatly improving upon other techniques for such data, even after giving faster methods equivalent computation (via more initializations).

The proposed method differs from existing work in two ways: a robust data fit model and a nested MM+ADMM algorithm for reconstruction with this model. Although this algorithm can be generalized, including to the conventional quadratic data fit term, preliminary experiments (not shown) do not portray the same level of robustness with the ℓ_2 approach as the proposed method with the ℓ_1 data fit term. Thus, the benefit likely derives from the data fit term. This hypothesis is consistent with the fact that competing methods perform well in settings without outliers. However, experimental results comparing the proposed algorithm to a conventional gradient method also suggest that the algorithm is important, as the gradient method converges very slowly and would not yield a quality result with the same amount of computation. Although existing methods may possess theoretic convergence guarantees, the faster empirical convergence of the objective function in (4) using the proposed method means that the model and algorithmic contributions are intertwined, and both are needed to achieve robustness with outliers. In SNR-limited applications like point spread function estimation in super-resolution optical microscopy, the additional robustness provided by the 1-norm model versus the Gaussian model will greatly simplify the acquisition and reduce noise-related errors in the phase retrieval reconstruction.

Some existing methods automatically tune parameters, like PR-GAMP [30]. With the normalization and adaptive methods for parameter selection we describe, the Monte Carlo simulations reveal significantly reduced errors versus other methods, even without extensive manual parameter tuning. A complete solution to parameter selection would rely on more

sophisticated automatic methods [69]. Further experiments on larger, real datasets are necessary to fully describe parameter selection and assess real performance of the proposed method.

Paired with parameter selection, multiple initializations are also important to overcome the nonconvexity of the inverse problem and find a reasonable global solution. Although recently proposed techniques like Wirtinger flow [70] show promise for the oversampled case, randomly selecting multiple initial majorization vectors s^0 appears to be more robust for the proposed method. As using multiple initial choices for s^0 proportionally increases computation time, the overall reconstruction time may be an issue in higher dimensions. However, a suitable 2D image reconstruction is obtained with the same number of initializations (50) as in the 1D case. Still, the 2D reconstructions all took over two hours on a modern workstation using MATLAB. Compared to much faster, simpler methods like alternating projections, that can recover an image in seconds or minutes (in the absence of outliers), the proposed method is suitable when obtaining a quality reconstruction is paramount, or when those faster methods fail to recover the true image (like in Figure 9).

In both the 1D and 2D cases, the proposed method clearly outperforms the L_1-modified sparse Fienup method, GESPAR, and even PR-GAMP, when outliers are present in the data, even when controlling for computation time. As the reduced squared error is prominent for the extremely sparse signals evaluated here, the 1-norm sparsity term should allow for similar improvements for signals that are less sparse or compressible. This quality gain is not without cost, as the mean squared error (in supplementary material) shows greater variability than the median numbers, suggesting noticeable errors are generally larger versus other methods. In the future, this framework will be extended to image domain constraints like nonnegativity and other forms of regularization, including analysis-form sparsity. These additions should facilitate reconstruction of real images.

VII. Conclusion

The key contributions of this paper are two-fold and intertwined. A general framework is proposed that extends phase retrieval reconstruction to measurements corrupted by outliers. A new implementation of this general framework is described featuring multiple initializations, majorization-minimization, and (preconditioned) ADMM. In addition, using normalization and existing adaptive heuristics, the proposed method is made robust without manual tuning as noise levels/types or numbers of outliers change. A direct comparison against competing methods establishes quantitative and visible advantages over existing methods, over a wide range of simulations.

Acknowledgments

The authors would like to acknowledge Yoav Shechtman for insights relating to phase retrieval and coherent diffraction imaging, and for sharing image data, and James Fienup for general discussions on phase retrieval. A special thanks also goes out to the reviewers, for providing substantive and constructive feedback on multiple iterations of this paper.

References

[1] J. R. Fienup, "Phase retrieval algorithms: A personal tour," *Appl. Opt.*, vol. 52, no. 1, pp. 45–56, Jan. 2013.
[2] Y. Shechtman, Y. C. Eldar, O. Cohen, H. N. Chapman, J. Miao, and M. Segev, "Phase retrieval with application to optical imaging: A contemporary overview," *IEEE Signal Process. Mag.*, vol. 32, no. 3, pp. 87–109, May 2015.
[3] M. V. Klibanov, P. E. Sacks, and A. V. Tikhonravov, "The phase retrieval problem," *Inverse Prob.*, vol. 11, no. 1, pp. 1–28, Feb. 1995.
[4] D. Sayre, "Some implications of a theorem due to Shannon," *Acta Crystallogr.*, vol. 5, p. 843, 1952.
[5] R. P. Millane, "Phase retrieval in crystallography and optics," *J. Opt. Soc. Amer. A*, vol. 7, no. 3, pp. 394–411, Mar. 1990.
[6] H. A. Hauptman, "The phase problem of X-ray crystallography," *Rep. Prog. Phys.*, vol. 54, no. 11, pp. 1427–1454, Nov. 1991.
[7] R. W. Harrison, "Phase problem in crystallography," *J. Opt. Soc. Amer. A*, vol. 10, no. 5, pp. 1046–1055, May 1993.
[8] A. Walther, "The question of phase retrieval in optics," *Opt. Acta Int. J. Opt.*, vol. 10, no. 1, pp. 41–49, 1963.
[9] J. R. Fienup and J. C. Dainty, "Phase retrieval and image reconstruction for astronomy," in *Image Recovery: Theory and Application*, H. Stark, Ed. New York, NY, USA: Academic, 1987, pp. 231–275.
[10] J. Miao, P. Charalambous, J. Kirz, and D. Sayre, "Extending the methodology of X-ray crystallography to allow imaging of micrometre-sized non-crystalline specimens," *Nature*, vol. 400, no. 6742, pp. 342–344, Jul. 1999.
[11] R. Balan, P. Casazza, and D. Edidin, "On signal reconstruction without phase," *Appl. Comput. Harmon. Anal.*, vol. 20, no. 3, pp. 345–356, May 2006.
[12] K. Setsompop, L. L. Wald, V. Alagappan, B. A. Gagoski, and E. Adalsteinsson, "Magnitude least squares optimization for parallel radio frequency excitation design demonstrated at 7 Tesla with eight channels," *Mag. Res. Med.*, vol. 59, no. 4, pp. 908–915, Apr. 2008.
[13] A. Chai, M. Moscoso, and G. Papanicolaou, "Array imaging using intensity-only measurements," *Inverse Prob.*, vol. 27, no. 1, p. 015005, Jan. 2011.
[14] T. Latychevskaia, J.-N. Longchamp, and H.-W. Fink, "Novel Fourier-domain constraint for fast phase retrieval in coherent diffraction imaging," *Opt. Express*, vol. 19, no. 20, pp. 19330–19339, Sep. 2011.
[15] A. V. Oppenheim and J. S. Lim, "The importance of phase in signals," *Proc. IEEE*, vol. 69, no. 5, pp. 529–541, May 1981.
[16] R. W. Gerchberg and W. O. Saxton, "A practical algorithm for the determination of phase from image and diffraction plane pictures," *Optik*, vol. 35, pp. 237–246, Apr. 1972.
[17] J. R. Fienup, "Reconstruction of an object from the modulus of its Fourier transform," *Opt. Lett.*, vol. 3, no. 1, pp. 27–29, Jul. 1978.
[18] J. R. Fienup, "Phase retrieval algorithms: A comparison," *Appl. Opt.*, vol. 21, no. 15, pp. 2758–2769, Aug. 1982.
[19] M. H. Hayes and T. F. Quatieri, "Recursive phase retrieval using boundary conditions," *J. Opt. Soc. Amer.*, vol. 73, no. 11, pp. 1427–1433, Nov. 1983.
[20] J. R. Fienup, "Phase retrieval using boundary conditions," *J. Opt. Soc. Amer. A*, vol. 3, no. 2, pp. 284–288, Feb. 1986.
[21] J. R. Fienup, "Reconstruction of a complex valued object from the modulus of its Fourier transform using a support constraint," *J. Opt. Soc. Amer. A*, vol. 4, no. 1, pp. 118–123, Jan. 1987.
[22] V. Elser, "Phase retrieval by iterated projections," *J. Opt. Soc. Amer. A*, vol. 20, no. 1, pp. 40–55, Jan. 2003.
[23] S. Marchesini, "A unified evaluation of iterative projection algorithms for phase retrieval," *Rev. Sci. Instrum.*, vol. 78, no. 1, p. 011301, Mar. 2007.
[24] S. Marchesini, "Phase retrieval and saddle-point optimization," *J. Opt. Soc. Amer. A*, vol. 24, no. 10, pp. 3289–3296, Oct. 2007.
[25] H. H. Bauschke, P. L. Combettes, and D. R. Luke, "Hybrid projection-reflection method for phase retrieval," *J. Opt. Soc. Amer. A*, vol. 20, no. 6, pp. 1025–1034, Jun. 2003.
[26] H. Ohlsson and Y. C. Eldar, "On conditions for uniqueness in sparse phase retrieval," in *Proc. IEEE Conf. Acoust. Speech Signal*, 2014, pp. 1841–1845.
[27] J. Ranieri, A. Chebira, Y. M. Lu, and M. Vetterli, "Phase retrieval for sparse signals: Uniqueness conditions," 2013 [Online]. Available: http://arxiv.org/abs/1308.3058
[28] Y. C. Eldar and S. Mendelson, "Phase retrieval: Stability and recovery guarantees," *Appl. Comput. Harmon. Anal.*, vol. 36, no. 3, pp. 473–494, May 2014.
[29] M. L. Moravec, J. K. Romberg, and R. G. Baraniuk, "Compressive phase retrieval," in *Proc. SPIE Wavelets XII*, 2007, p. 670120.

[30] P. Schniter and S. Rangan, "Compressive phase retrieval via generalized approximate message passing," in *Proc. 50th Allerton Conf. Commun. Control Comput.*, 2012, pp. 815–822.
[31] S. Mukherjee and C. S. Seelamantula, "An iterative algorithm for phase retrieval with sparsity constraints: Application to frequency domain optical coherence tomography," in *Proc. IEEE Conf. Acoust. Speech Signal.*, 2012, pp. 553–556.
[32] E. Osherovich, M. Zibulevsky, and I. Yavneh, "Approximate fourier phase information in the phase retrieval problem: What it gives and how to use it," *J. Opt. Soc. Amer. A*, vol. 28, no. 10, pp. 2124–2131, Oct. 2011.
[33] E. J. Candès, T. Strohmer, and V. Voroninski, "PhaseLift: Exact and stable signal recovery from magnitude measurements via convex programming," *Commun. Pure Appl. Math.*, vol. 66, no. 8, pp. 1241–1274, Aug. 2013.
[34] E. J. Candès, Y. C. Eldar, T. Strohmer, and V. Voroninski, "Phase retrieval via matrix completion," *SIAM J. Imag. Sci.*, vol. 6, no. 1, pp. 199–225, 2013.
[35] L. Demanet and V. Jugnon, "Convex recovery from interferometric measurements," 2013 [Online]. Available: http://arxiv.org/abs/1307.6864
[36] Y. Shechtman, Y. C. Eldar, A. Szameit, and M. Segev, "Sparsity based sub-wavelength imaging with partially incoherent light via quadratic compressed sensing," *Opt. Express*, vol. 19, no. 16, pp. 14807–14822, Aug. 2011.
[37] H. Ohlsson, A. Y. Yang, R. Dong, and S. S. Sastry, "Compressive phase retrieval from squared output measurements via semidefinite programming," 2012 [Online]. Available: http://arxiv.org/abs/1111.6323
[38] X. Li and V. Voroninski, "Sparse signal recovery from quadratic measurements via convex programming," *SIAM J. Math. Anal.*, vol. 45, no. 5, pp. 3019–3033, 2013.
[39] I. Waldspurger, A. D'Aspremont, and S. Mallat, "Phase recovery, MaxCut and complex semidefinite programming," *Math. Programm.*, vol. 149, no. 1, pp. 47–81, Feb. 2015.
[40] E. J. Candès and X. Li, "Solving quadratic equations via PhaseLift when there are about as many equations as unknowns," *Found. Comput. Math.*, vol. 14, no. 5, pp. 1017–1026, 2014.
[41] P. Hand, "PhaseLift is robust to a constant fraction of arbitrary errors," 2015[Online]. Available: http://arxiv.org/abs/1502.04241v1
[42] K. Jaganathan, S. Oymak, and B. Hassibi, "Recovery of sparse 1-D signals from the magnitudes of their Fourier transform," in *Proc. Int. Symp. Inf. Theory*, 2012, pp. 1473–1477.
[43] Y. Shechtman, A. Beck, and Y. C. Eldar, "GESPAR: Efficient phase retrieval of sparse signals," *IEEE Trans. Signal Process.*, vol. 62, no. 4, pp. 928–938, Feb. 2014.
[44] D. S. Weller, A. Pnueli, O. Radzyner, G. Divon, Y. C. Eldar, and J. A. Fessler, "Phase retrieval of sparse signals using optimization transfer and ADMM," in *Proc. IEEE Int. Conf. Image Process.*, 2014, pp. 1342–1346.
[45] S. Boyd, N. Parikh, E. Chu, B. Peleato, and J. Eckstein, "Distributed optimization and statistical learning via the alternating direction method of multipliers," *Found. Trends Mach. Learn.*, vol. 3, no. 1, pp. 1–122, 2010.
[46] R. Tibshirani, "Regression shrinkage and selection via the LASSO," *J. Roy. Statist. Soc. Ser. B*, vol. 58, no. 1, pp. 267–288, 1996.
[47] R. Fletcher and C. M. Reeves, "Function minimization by conjugate gradients," *Comput. J.*, vol. 7, no. 2, pp. 149–154, 1964.
[48] M. W. Jacobson and J. A. Fessler, "An expanded theoretical treatment of iteration-dependent majorize-minimize algorithms," *IEEE Trans. Image Process.*, vol. 16, no. 10, pp. 2411–2422, Oct. 2007.
[49] S. Boyd and L. Vandenberghe, *Convex Optimization*. Cambridge, U.K.: Cambridge Univ. Press, 2004.
[50] A. L. Yuille and A. Rangarajan, "The concave-convex procedure," *Neural Comput.*, vol. 15, no. 4, pp. 915–936, Apr. 2003.
[51] K. Kim, Y. D. Son, Y. Bresler, Z. H. Cho, J. B. Ra, and J. C. Ye, "Dynamic PET reconstruction using temporal patch-based low rank penalty for ROI-based brain kinetic analysis," *Phys. Med. Biol.*, vol. 60, no. 5, p. 2019, Mar. 2015.
[52] K. Lange, D. R. Hunter, and I. Yang, "Optimization transfer using surrogate objective functions," *J. Comput. Graph. Statist.*, vol. 9, no. 1, pp. 1–20, Mar. 2000.
[53] R. Glowinski and A. Marrocco, "Sur l'approximation, par éléments finis d'ordre un, et la résolution, par pénalisation-dualité d'une classe de problèmes de dirichlet non linéaires," *Modél. Math. Anal. Numér.*, vol. 9, no. R2, pp. 41–76, 1975.
[54] D. Gabay and B. Mercier, "A dual algorithm for the solution of nonlinear variational problems via finite-element approximations," *Comput. Math. Appl.*, vol. 2, no. 1, pp. 17–40, 1976.
[55] J. Eckstein and D. P. Bertsekas, "On the Douglas-Rachford splitting method and the proximal point algorithm for maximal monotone operators," *Math. Programm.*, vol. 55, no. 1–3, pp. 293–318, Apr. 1992.
[56] S. S. Chen, D. L. Donoho, and M. A. Saunders, "Atomic decomposition by basis pursuit," *SIAM J. Sci. Comput.*, vol. 20, no. 1, pp. 33–61, 1998.
[57] D. L. Donoho and M. Elad, "Optimally sparse representation in general (nonorthogonal) dictionaries via 1 minimization," *Proc. Nat. Acad. Sci.*, vol. 100, no. 5, pp. 2197–2202, Mar. 2003.
[58] J. A. Tropp, "Greed is good: Algorithmic results for sparse approximation," *IEEE Trans. Inf. Theory*, vol. 50, no. 10, pp. 2231–2242, Oct. 2004.
[59] Y. Eldar and G. Kutyniok, *Compressed Sensing: Theory and Applications*. Cambridge, U.K.: Cambridge Univ. Press, 2012.
[60] A. Beck and M. Teboulle, "A fast iterative shrinkage-thresholding algorithm for linear inverse problems," *SIAM J. Imag. Sci.*, vol. 2, no. 1, pp. 183–202, 2009.
[61] A. Chambolle and T. Pock, "A first-order primal-dual algorithm for convex problems with applications to imaging," *J. Math. Imag. Vis.*, vol. 40, no. 1, pp. 120–145, 2011.
[62] Y. Ouyang, Y. Chen, G. Lan, and E. Pasiliao Jr., "An accelerated linearized alternating direction method of multipliers," *SIAM J. Imag. Sci.*, vol. 8, no. 1, pp. 644–681, 2015.
[63] T. Goldstein, B. O'Donoghue, and S. Setzer, "Fast alternating direction optimization methods," *SIAM J. Imag. Sci.*, vol. 7, no. 3, pp. 1588–1623, 2014.
[64] Y. Nesterov, "A method of solving a convex programming problem with convergence rate $O(1/k^2)$," *Soviet Math. Doklady*, vol. 27, no. 2, pp. 372–376, 1983.
[65] B. O'Donoghue and E. Candès, "Adaptive restart for accelerated gradient schemes," *Found. Comput. Math.*, vol. 15, no. 3, pp. 715–732, Jun. 2015.
[66] M. Fazel, T. K. Pong, D. Sun, and P. Tseng, "Hankel matrix rank minimization with applications to system identification and realization," *SIAM J. Matrix. Anal. Appl.*, vol. 34, no. 3, pp. 946–977, 2013.
[67] E. Ghadimi, A. Teixeira, I. Shames, and M. Johansson, "Optimal parameter selection for the alternating direction method of multipliers (ADMM): Quadratic problems," *IEEE Trans. Autom. Control*, vol. 60, no. 3, pp. 644–658, Mar. 2015.
[68] A. Szameit *et al.*, "Sparsity-based single-shot subwavelength coherent diffractive imaging," *Nat. Mater.*, vol. 11, p. 455, Apr. 2012.
[69] D. S. Weller, S. Ramani, J.-F. Nielsen, and J. A. Fessler, "Monte carlo SURE-based parameter selection for parallel magnetic resonance imaging reconstruction," *Magn. Res. Med.*, vol. 71, no. 5, pp. 1760–1770, May 2014.
[70] E. J. Candès, X. Li, and M. Soltanolkotabi, "Phase retrieval via wirtinger flow: Theory and algorithms," *IEEE Trans. Inf. Theory*, vol. 61, no. 4, pp. 1985–2007, Apr. 2015.

Daniel S. Weller (S'05–M'12) received the B.S. degree in electrical and computer engineering (with Hons.), from Carnegie Mellon University, Pittsburgh, PA, USA, the S.M. and Ph.D. degrees in electrical engineering from the Massachusetts Institute of Technology, Cambridge, MA, USA, in May 2006, June 2012, and June 2008, respectively. He worked with the Signal Transformation and Information Representation Group, Research Laboratory of Electronics, Massachusetts Institute of Technology, Cambridge, MA, USA. He joined the University of Virginia, Charlottesville, VA, USA, in August 2014, where he is an Assistant Professor of Electrical and Computer Engineering, with courtesy appointments in Biomedical Engineering and in Radiology and Medical Imaging. From 2012 to 2014, he was a Postdoctoral Research Fellow in the Electrical Engineering—Systems Program with the University of Michigan, Ann Arbor, MI, USA, supported by the National Institutes of Health via a Ruth L. Kirschstein National Research Service Award. He was a Research Assistant with the General Motors Collaborative Research Laboratory, Carnegie Mellon, Pittsburgh, PA, USA. He also worked with Texas Instruments, Apple, and ATK. His research interests include medical imaging, especially magnetic resonance imaging, signal processing and estimation, and nonideal sampling and reconstruction. He is a Member of Tau Beta Pi, Eta Kappa Nu, and the International Society for Magnetic Resonance in Medicine (ISMRM). He currently serves as an Associate Editor for the IEEE TRANSACTIONS ON MEDICAL IMAGING, and has reviewed for numerous IEEE and other professional journals and conferences. He was a Finalist in the Student Paper Competition at the 2011

IEEE International Symposium on Biomedical Imaging. He was the recipient of the National Defense Science and Engineering Graduate Fellowship and a Graduate Research Fellowship from the National Science Foundation.

Ayelet Pnueli received the Ph.D. degree in physics from the Technion (Israel Institute of Technology), Haifa, Israel. She worked many years in various R&D positions in the industry including IAI (Israeli aircraft industry), Applied Materials Inc., and HP Labs. Currently, she is a Designer of digital educational games.

Gilad Divon received the B.Sc. degree in electrical engineering and the B.A. degree in physics from the Technion (Israel Institute of Technology), Haifa, Israel, in 2015. Currently, he is pursuing the Master's degree in electrical engineering in the field of computer vision and graphic, dealing with saliency of 3D models. He also worked as a Student and as a System Engineer with Elbit Systems Ltd, Haifa, Israel, in the civil aviation, the electro-optical R&D groups.

Ori Radzyner received the B.Sc degree in electrical engineering and the B.A degree in physics from the Technion (Israel Institute of Technology), in Haifa, Israel, in 2015. He worked as a Student at Elbit Systems Ltd. in one of the electro-optical R&D groups. Currently, he works as an Engineer in the Semiconductor Industry.

Yonina C. Eldar (S'98–M'02–SM'07–F'12) received the B.Sc. degree in physics, and the B.Sc. degree in electrical engineering from Tel-Aviv University (TAU), Tel-Aviv, Israel, and the Ph.D. degree in electrical engineering and Computer Science from the Massachusetts Institute of Technology (MIT), Cambridge, MA, USA, in 1995, 1996, and 2002, respectively. From January 2002 to July 2002, she was a Postdoctoral Fellow with the Digital Signal Processing Group at MIT. She is currently a Professor of Electrical Engineering with the Technion—Israel Institute of Technology, Haifa, Israel, where she holds the Edwards Chair in Engineering. She is also a Research Affiliate with the Research Laboratory of Electronics, MIT, and was a Visiting Professor at Stanford University, Stanford, CA, USA. Her research interests include statistical signal processing, sampling theory and compressed sensing, optimization methods, and their applications to biology and optics. She is author of the book *Sampling Theory: Beyond Bandlimited Systems,* and co-author of the books *Compressed Sensing* and *Convex Optimization Methods in Signal Processing and Communications* (Cambridge University Press). She is a member of the Young Israel Academy of Science and Humanities and the Israel Committee for Higher Education. She is the Editor-in-Chief of *Foundations and Trends in Signal Processing*, a member of the IEEE Sensor Array and Multichannel Technical Committee and serves on several other IEEE committees. In the past, she was a Signal Processing Society Distinguished Lecturer, member of the IEEE Signal Processing Theory and Methods and Bio Imaging Signal Processing technical committees, and served as an Associate Editor for the IEEE TRANSACTIONS ON SIGNAL PROCESSING, the *EURASIP Journal of Signal Processing*, the *SIAM Journal on Matrix Analysis and Applications*, and the *SIAM Journal on Imaging Sciences*. She was a Co-Chair and Technical Co-Chair of several international conferences and workshops. She was selected as one of the 50 most influential women in Israel. She was a Horev Fellow of the Leaders in Science and Technology program at the Technion and an Alon Fellow. She was the recipient of numerous awards for excellence in research and teaching, including the IEEE Signal Processing Society Technical Achievement Award (2013), the IEEE/AESS Fred Nathanson Memorial Radar Award (2014), and the IEEE Kiyo Tomiyasu Award (2016). She was also the recipient of the Michael Bruno Memorial Award from the Rothschild Foundation, the Weizmann Prize for Exact Sciences, the Wolf Foundation Krill Prize for Excellence in Scientific Research, the Henry Taub Prize for Excellence in Research (twice), the Hershel Rich Innovation Award (three times), the Award for Women with Distinguished Contributions, the Andre and Bella Meyer Lectureship, the Career Development Chair at the Technion, the Muriel and David Jacknow Award for Excellence in Teaching, and the Technions Award for Excellence in Teaching (2 times). She was the recipient of the several best paper awards and best demo awards together with her research students and colleagues including the SIAM outstanding Paper Prize and the IET Circuits, Devices, and Systems Premium Award.

Jeffrey A. Fessler (F'06) received the B.S.E.E. degree from Purdue University, West Lafayette, IN, USA, and the M.S.E.E. degree, the M.S. degree in statistics, and the Ph.D. degree in electrical engineering from Stanford University, Stanford, CA, USA, in 1985, 1986, 1989, and 1990, respectively. From 1985 to 1988, he was a National Science Foundation Graduate Fellow at Stanford. Since 1990, he has been with the University of Michigan, Ann Arbor, MI, USA, where he was a Department of Energy Alexander Hollaender Postdoctoral Fellow in the Division of Nuclear Medicine from 1991 to 1992, and an Assistant Professor of Nuclear Medicine and the Bioengineering Program from 1993 to 1995. He is currently a Professor with the Departments of Electrical Engineering and Computer Science, Radiology, and Biomedical Engineering. His research interests include statistical aspects of imaging problems. He has supervised doctoral research in PET, SPECT, X-ray CT, MRI, and optical imaging problems. He has served as an Associate Editor for the IEEE TRANSACTIONS ON MEDICAL IMAGING, the IEEE SIGNAL PROCESSING LETTERS, and the IEEE TRANSACTIONS ON IMAGE PROCESSING, and is currently serving as an Associate Editor for the IEEE TRANSACTIONS ON COMPUTATIONAL IMAGING. He has chaired the IEEE T-MI Steering Committee and the ISBI Steering Committee. He was a Co-Chair of the 1997 SPIE conference on Image Reconstruction and Restoration, Technical Program Co-Chair of the 2002 IEEE International Symposium on Biomedical Imaging (ISBI), and General Chair of ISBI 2007. He was the recipient of the Francois Erbsmann Award for his IPMI93 presentation, and the Edward Hoffman Medical Imaging Scientist Award in 2013.

Undersampled Phase Retrieval with Outliers: Supplementary Material

Daniel S. Weller, *Member, IEEE,* Ayelet Pnueli, Gilad Divon, Ori Radzyner,
Yonina C. Eldar, *Fellow, IEEE,* and Jeffrey A. Fessler, *Fellow, IEEE*

Here we provide additional mathematical details for the $\boldsymbol{u}$ update step with different data fit terms and additional experimental support related to the paper [1].

I. Updating u : Squared-Magnitude Measurements, Laplace Data Fit Term

In this case, $f(\cdot) = (\cdot)$, and $q = 2$. When $y_m < 0$, $f_+(u)$ is always greater than $f_-(u)$, so the solution is always the minimizer of $f_+(u)$. Otherwise, we must consider all three cases.

Let $d = [\boldsymbol{A}\boldsymbol{x}^{i+1} + \boldsymbol{b}^i]_m$, s represent the appropriate choice of s_m or $\bar{s}_m$, $\eta \triangleq \mu/2$, and drop the subscripts. Writing out $f_+(u)$ and $f_-(u)$,

$$f_+(u) = \eta|u-d|^2 + |u|^2 - y,$$
$$f_-(u) = \eta|u-d|^2 + y + |s|^2 - 2|s|\mathcal{R}\mathrm{e}\{ue^{-\imath\angle s}\}.$$

The function $f_+(u)$ is quadratic in u; differentiating yields

$$\frac{df_+(u)}{du} = 2\eta(u-d) + 2u.$$

Thus, $f_+(u)$ is minimized by $u_+ = \frac{\eta}{1+\eta}d$.

The function $f_-(u)$ is also a quadratic, so

$$\frac{df_-(u)}{du} = 2\eta(u-d) - 2s,$$

which set to zero yields the minimizer $u_- = \frac{s}{\eta} + d$.

The minimization of $f_+(u)$ or $f_-(u)$ along the curve on which both functions are equal-valued, involves parameterizing this curve and minimizing $f_+(u)$ as a function of this parameter. These functions are equal when $|u|^2 - y = y + |s|^2 - 2|s|\mathcal{R}\mathrm{e}\{ue^{-\imath\angle s}\}$, which corresponds to the circle $|u+s|^2 = 2(y+|s|^2)$. The parameterization then corresponds to the angle along the circle; call it θ. The curve of interest is $(u+s) = \sqrt{2(y+|s|^2)}e^{\imath\theta}$. Incorporating this parameterization into $f_+(u)$ yields

$$f_+(u(\theta)) = -2\sqrt{2(y+|s|^2)}\mathcal{R}\mathrm{e}\{((1+\eta)s + \eta d)e^{-\imath\theta}\} + \text{constants},$$

which is minimized when $\theta = \angle((1+\eta)s + \eta d)$. So, $u_\pm = \sqrt{2(y+|s|^2)}e^{\imath\angle((1+\eta)s+\eta d)} - s$.

DSW was funded by National Institutes of Health (NIH) grant F32 EB015914. JAF is funded in part by NIH grant U01 EB018753 and an equipment donation from Intel. YCE is funded in part by Israel Science Foundation Grant 170/10, SRC, and Intel Collaborative Research Institute for Computational Intelligence.

DSW is with the Charles L. Brown Department of Electrical and Computer Engineering, University of Virginia, Charlottesville, VA 22904 USA (email: dweller@virginia.edu). AP was with, and GD, OR, and YCE are with the Electrical Engineering Department, Technion, Israel Institute of Technology, Haifa 32000, Israel (emails: ayelet.pnueli@gmail.com, giladd44@gmail.com, radzy@campus.technion.ac.il, yonina@ee.technion.ac.il). JAF is with the Department of Electrical Engineering and Computer Science, University of Michigan, Ann Arbor, MI 48109 USA (email: fessler@umich.edu).

II. Updating u : Squared-Magnitude Measurements, Gaussian Data Fit Term

In this case, $f(\cdot) = (\cdot)^2$, and $q = 2$. Again, as with the Laplace data fit term, when $y_m < 0$, $f_+(u) > f_-(u)$, so we always minimize $f_+(u)$. Otherwise, we consider all three cases.

Again, let $d = [\boldsymbol{A}\boldsymbol{x}^{i+1} + \boldsymbol{b}^i]_m$, s represent the appropriate choice of s_m or $\bar{s}_m$, $\eta \triangleq \mu/2$, and drop the subscripts. Writing out $f_+(u)$ and $f_-(u)$,

$$\begin{aligned} f_+(u) &= \eta|u-d|^2 + (|u|^2 - y)^2, \\ f_-(u) &= \eta|u-d|^2 + (y + |s|^2 - 2|s|\mathcal{R}\mathrm{e}\{ue^{-\imath\angle s}\})^2. \end{aligned}$$

Writing $f_+(u)$ in terms of the magnitude $|u|$ and phase $\angle u$ of u,

$$\begin{aligned} f_+(u) = \eta|u|^2 + \eta|d|^2 - 2\eta|u||d|\cos(\angle u - \angle d) \\ + |u|^4 - 2y|u|^2 + y^2, \end{aligned}$$

which is clearly minimized when $\angle u = \angle d$, when $\cos(\angle u - \angle d) = 1$. Then, $f_+(u)$ becomes a quartic equation in $|u|$, which has the derivative

$$\frac{df_+(u)}{d|u|} = 4|u|^3 + (2\eta - 4y)|u| - 2\eta|d|.$$

The function $f_+(u)$ is minimized either when the derivative is zero or when $|u| = 0$. The depressed cubic equation will have between zero and three nonnegative real roots, which can be found analytically. Note that if there are three positive real roots, since the cubic must be increasing below the least positive root, the derivative at $|u| = 0$ is negative, and the fourth candidate point $|u| = 0$ cannot be the global minimum. The minimizer u_+ is the candidate point with minimum function value $f_+(|u|)$, multiplied by $e^{\imath\angle d}$.

Finding a minimum of $f_-(u)$ is straightforward. Define $\bar{u} = ue^{-\imath\angle s}$, and $\bar{d} = de^{-\imath\angle s}$. Then,

$$f_-(\bar{u}) = \eta|\bar{u} - \bar{d}|^2 + (y + |s|^2 - 2|s|\mathcal{R}\mathrm{e}\{\bar{u}\})^2.$$

Separating the real and imaginary parts, we observe

$$\begin{aligned} f_-(\bar{u}) = \eta(\mathcal{R}\mathrm{e}\{\bar{u}\} - \mathcal{R}\mathrm{e}\{\bar{d}\})^2 + \eta(\mathcal{I}\mathrm{m}\{\bar{u}\} - \mathcal{I}\mathrm{m}\{\bar{d}\})^2 \\ + (y + |s|^2 - 2|s|\mathcal{R}\mathrm{e}\{\bar{u}\})^2, \end{aligned}$$

which is clearly minimized when $\mathcal{I}\mathrm{m}\{\bar{u}\} = \mathcal{I}\mathrm{m}\{\bar{d}\}$. The real component is quadratic in $\mathcal{R}\mathrm{e}\{\bar{u}\}$, so differentiating with respect to $\mathcal{R}\mathrm{e}\{\bar{u}\}$ yields

$$\begin{aligned} \frac{df_+(\bar{u})}{d\mathcal{R}\mathrm{e}\{\bar{u}\}} = 2\eta(\mathcal{R}\mathrm{e}\{\bar{u}\} - \mathcal{R}\mathrm{e}\{\bar{d}\}) \\ + 4|s|(2|s|\mathcal{R}\mathrm{e}\{\bar{u}\} - (y + |s|^2)), \end{aligned}$$

which is minimized at

$$\mathcal{R}\mathrm{e}\{\bar{u}\} = \frac{\eta\mathcal{R}\mathrm{e}\{\bar{d}\} + 2|s|(y + |s|^2)}{\eta + 4|s|^2}.$$

This closed form solution yields

$$u_- = (\mathcal{R}\mathrm{e}\{\bar{u}\} + \imath\mathcal{I}\mathrm{m}\{\bar{u}\})e^{\imath\angle s}.$$

Minimizing $f_+(u)$ along the curve $f_+(u) = f_-(u)$ requires parameterizing the curve. Again, define $\bar{u} = ue^{-\imath\angle s}$, $\bar{d} = de^{-\imath\angle s}$, and $\bar{s} = |s|$. Note that $\phi_-(\bar{u}; \bar{s}, y) = |\bar{s} - \bar{u}|^2 + (y - |\bar{u}|^2)$, where the latter term equals $B \triangleq -h_+(\bar{u}; y)$. Along the curve $f_+(\bar{u}) = f_-(\bar{u})$, $B^2 = (B + |\bar{s} - \bar{u}|^2)^2$, which is true when $s = \bar{u}$, or when $|\bar{s} - \bar{u}|^2 = -2B = 2(|\bar{u}|^2 - y)$. For this second case to yield a nontrivial solution requires $B < 0$, which corresponds to $|\bar{u}|^2 > y$.

Rearranging terms yields our familiar circle $|\bar{u} + \bar{s}|^2 = 2(y + \bar{s}^2)$ from the Laplace distribution case. Plugging our angular parameterization $\bar{u} = c_0 e^{\imath\theta} - s$, where $c_0 = \sqrt{2(y + \bar{s}^2)}$, into $f_+(\bar{u})$ yields

$$\begin{aligned} f_+(\bar{u}(\theta)) &= (|c_0 e^{\imath\theta} - \bar{s}|^2 - y)^2 + \eta|c_0 e^{\imath\theta} - \bar{s} - \bar{d}|^2 \\ &= (c_0^2 - 2c_0\mathcal{R}\mathrm{e}\{e^{\imath\theta}\bar{s}^*\} + \bar{s}^2 - y)^2 \\ &\quad + \eta(c_0^2 + |\bar{s} + \bar{d}|^2 - 2c_0\mathcal{R}\mathrm{e}\{e^{i\theta}(\bar{s} + \bar{d})^*\}). \end{aligned}$$

Let $c_1 = c_0^2 + \bar{s}^2 - y$, and $c_2 = c_0^2 + |\bar{s} + \bar{d}|^2$, so

$$\begin{aligned} f_+(\bar{u}(\theta)) &= (c_1 - 2c_0\mathcal{R}\mathrm{e}\{e^{\imath\theta}\bar{s}^*\})^2 \\ &\quad + \eta(c_2 - 2c_0\mathcal{R}\mathrm{e}\{e^{\imath\theta}(\bar{s}+\bar{d})^*\}) \\ &= (2c_0)^2\mathcal{R}\mathrm{e}\{e^{\imath\theta}\bar{s}^*\}^2 \\ &\quad - 2c_0\mathcal{R}\mathrm{e}\{e^{\imath\theta}(2c_1\bar{s} + \eta(\bar{s}+\bar{d}))^*\} + c_1^2 + \eta c_2. \end{aligned}$$

For convenience, let $r_1 = 2c_0\bar{s}$, and r_2 and α be the magnitude and phase of $2c_0(2c_1\bar{s} + \eta(\bar{s}+\bar{d}))$. Differentiating with respect to θ,

$$\frac{df_+(\bar{u}(\theta))}{d\theta} = r_2\sin(\theta - \alpha) - 2r_1^2\sin\theta\cos\theta.$$

Setting the derivative equal to zero,

$$\tfrac{r_2}{r_1^2}\sin(\theta-\alpha) = \sin(2\theta).$$

Defining ξ such that $\theta = 2\arctan\xi$, we have $\sin\theta = \sin(2\arctan\xi) = \frac{2\xi}{1+\xi^2}$, and $\cos\theta = \cos(2\arctan\xi) = \frac{1-\xi^2}{1+\xi^2}$. Thus,

$$\begin{aligned} \sin(2\theta) &= 2\tfrac{2\xi(1-\xi^2)}{(1+\xi^2)^2}, \\ \sin(\theta-\alpha) &= \tfrac{2\xi\cos\alpha - (1-\xi^2)\sin\alpha}{1+\xi^2}. \end{aligned}$$

Substituting,

$$\begin{aligned} 0 &= \tfrac{r_2}{r_1^2}(2\xi\cos\alpha - (1-\xi^2)\sin\alpha)(1+\xi^2) - 4\xi(1-\xi^2) \\ &= \tfrac{r_2}{r_1^2}(2\xi\cos\alpha + 2\xi^3\cos\alpha - \sin\alpha + \xi^4\sin\alpha) \\ &\quad - 4\xi(1-\xi^2) \\ &= (\tfrac{r_2}{r_1^2}\sin\alpha)\xi^4 + (2\tfrac{r_2}{r_1^2}\cos\alpha + 4)\xi^3 \\ &\quad + (2\tfrac{r_2}{r_1^2}\cos\alpha - 4)\xi - \tfrac{r_2}{r_1^2}\sin\alpha. \end{aligned}$$

This quartic equation can be solved analytically; the real root that corresponds to θ with the minimum $f_+(\bar{u}(\theta))$ is used to generate $u_\pm = (c_0 e^{\imath\theta} - \bar{s})e^{\imath\angle s}$, which is valid as long as $|u_\pm|^2 > y$. Also, one must consider $\theta = \pm\pi$, which correspond to $\xi = \pm\infty$, in case either extreme point minimizes $f_+(\bar{u}(\theta))$.

III. Additional Monte Carlo (1D) Simulations

In [1], we ran 50-trial Monte Carlo simulations to characterize the reconstruction quality of the proposed and competing methods. Those simulations employed 128-element signal vectors with sparsities K ranging from 3 to 8, and sampled noisy squared-magnitude measurements of these signals with 5 outliers and either Gaussian or Laplace noise (both 40 dB SNR). In addition to the median squared error values reported in the paper, we provide mean squared error values (still via PSER, in dB) in Figures 1–2 for the four methods. Note the proposed method still outperforms the competing methods, but the trend as K/N or M/N varies appears much less stable. This instability versus the median value is due to outliers in reconstruction quality where the best minimum identified did not correlate with the true signal.

The paper also explores trends in reconstruction quality as a function of the number of outliers and additive noise SNR, demonstrating that the proposed method achieves significantly greater median PSER than competing methods over a wide range of outliers and noise levels. Here, we include similar results for alternate sparsity levels K demonstrating similar advantages as outliers increase (Figure 3) and as noise levels change (Figure 4). The trends in mean PSER values (not shown) are similar, with the same variability depicted in the trends in mean squared error shown for measurements and sparsity in Figures 1 and 2.

In addition to all these experiments comparing against GESPAR, PR-GAMP, and L1-Fienup, the proposed method is compared against the compressive phase retrieval (CPRL) method in [2], for a length-64 one-dimensional signal. The CPRL implementation from http://users.isy.liu.se/en/rt/ohlsson/code.html uses the standard CVX toolbox from http://cvxr.com/cvx/ with included semidefinite program solver SDPT3. This solver uses > 17 GB of memory

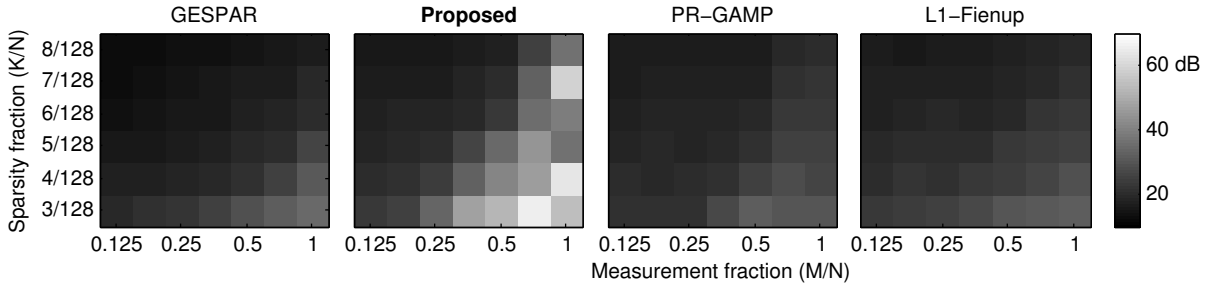

Fig. 1. The mean PSERs for 50 trials reconstructed using GESPAR, the proposed method, PR-GAMP, and L_1-Fienup, for a range of measurement (M/N) and sparsity fractions (K/N), for measurements with 40 dB SNR Gaussian noise and 5 outliers.

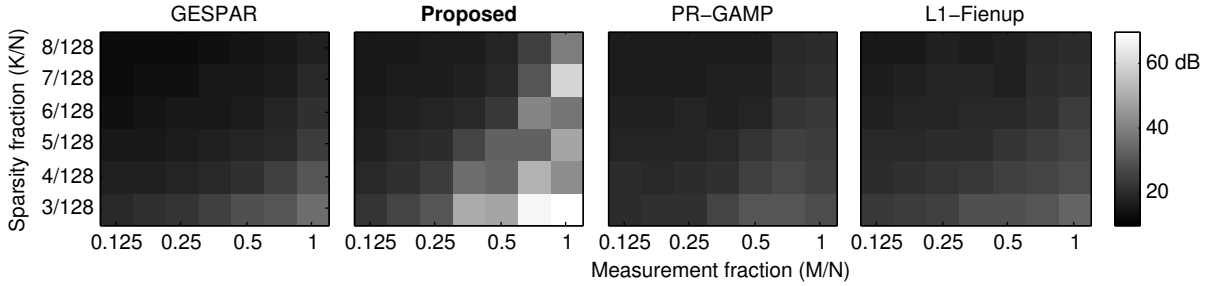

Fig. 2. The mean PSERs for 50 trials reconstructed using GESPAR, the proposed method, PR-GAMP, and L_1-Fienup, for a range of measurement (M/N) and sparsity fractions (K/N), for measurements with 40 dB SNR Laplace noise and 5 outliers.

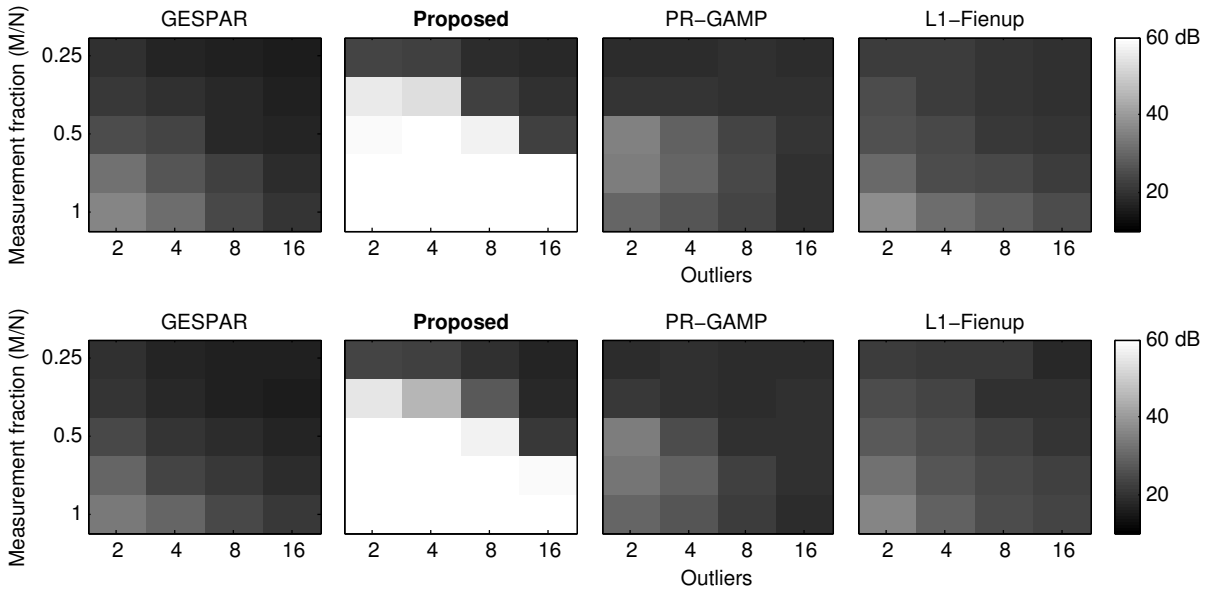

Fig. 3. The PSER of 50 trials reconstructed using GESPAR, the proposed method, PR-GAMP, and L_1-Fienup, for a range of measurement (M/N) and outliers, for $K = 5$ and measurements with 40 dB SNR Gaussian noise. The top and bottom rows display results for outliers with ranges $[1, \sqrt{2}]$ and $[1, 2]$, respectively.

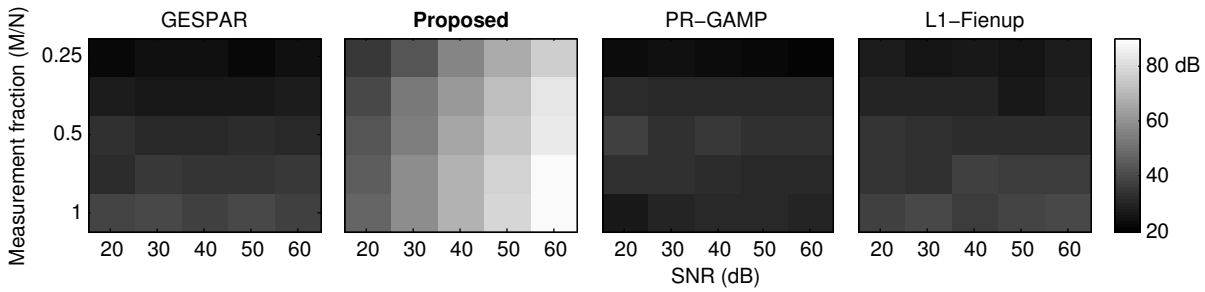

Fig. 4. The PSER of 50 trials reconstructed using GESPAR, the proposed method, PR-GAMP, and L_1-Fienup, for a range of measurement (M/N) and Gaussian noise SNRs, for $K = 3$ and measurements with 5 outliers (range $[1, 2]$).

for a length-128 signal, necessitating a smaller problem for this experiment. This simulation also uses a different sensing matrix $\boldsymbol{A}$, with a random Gaussian matrix multiplying the DFT. Tailoring the error bound ϵ to the true error in the measurements, and hand-tuning the best regularization parameter λ for CPRL's 1-norm sparsity term, the CPRL method is run for a range of sparsities K and measurements M corrupted with 40 dB SNR Gaussian noise and $0 - 2$ outliers. The median squared error is compared against the proposed method for the same signals, and the results are shown in Figure 5. The proposed method remains robust in the presence of outliers, while the compressive matrix lifting method does not.

IV. Additional Image Comparisons (2D)

The image comparisons in [1] demonstrate the superior reconstruction quality of the proposed method when the number of outliers is a sizable fraction (1%) of the measurements. The reconstructions in Figure 6 portray the degradation in image quality of the competing methods, as opposed to the consistent quality of the proposed method, as the number of outliers rises from negligible ($0.001\% = 2$) to more significant ($0.1\% = 132$). Although each set of results corresponds to one trial, the proposed method consistently outputs the star of David phantom, with only nominal gain differences in a few discs. The GESPAR method actually succeeds the best of any competing method, reproducing the star of David shape with only mild attenuation errors when few outliers are present. However, when outliers are more significant, GESPAR's performance degrades noticeably. The PR-GAMP method tends to fail to reconstruct the phantom, although the image for 0.001% outliers appears to bear a faint resemblance to the phantom. The L_1-Fienup method performs reasonably well when outliers are negligible, but it appears less stable than GESPAR or the proposed method as the number of outliers increases. As in the paper, these reconstructions of the $N = 512 \times 512$ star of David image (inspired by related work [3]) are all from $M = N/2 = 131,072$ measurements with outliers and 60 dB SNR additive white Gaussian noise, and the reconstructions all use the same 512×512 atom dictionary of discs 21 pixels wide as the synthesis transform. The same parameter value $\beta = 0.3$ used for the proposed method with 1% outliers in the paper is used here as well, suggesting that additional parameter tuning is unnecessary over a wide range of outliers. Again, the competing methods are run for at least as many (often many more) initializations and computations as the proposed method for fairness.

References

[1] D. S. Weller, A. Pnueli, G. Divon, O. Radzyner, Y. C. Eldar, and J. A. Fessler, "Undersampled phase retrieval with outliers," *IEEE Trans. Comput. Imag.*, accepted.

[2] H. Ohlsson, A. Y. Yang, R. Dong, and S. S. Sastry, "Compressive phase retrieval from squared output measurements via semidefinite programming," 2012, arxiv 1111.6323. [Online]. Available: http://arxiv.org/abs/1111.6323

[3] A. Szameit, Y. Shechtman, E. Osherovich, E. Bullkich, P. Sidorenko, H. Dana, S. Steiner, E. B. Kley, S. Gazit, T. Cohen-Hyams, S. Shoham, M. Zibulevsky, I. Yavneh, Y. C. Eldar, O. Cohen, and M. Segev, "Sparsity-based single-shot subwavelength coherent diffractive imaging," *Nature Materials*, vol. 11, p. 4559, Apr. 2012.

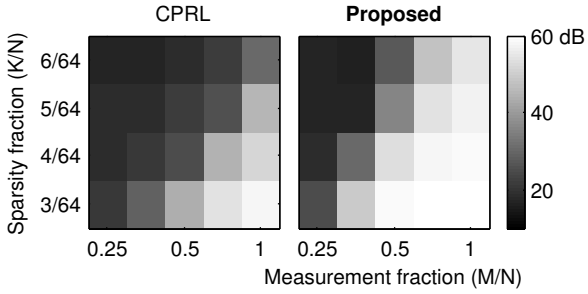

(a) 40 dB SNR AWGN only

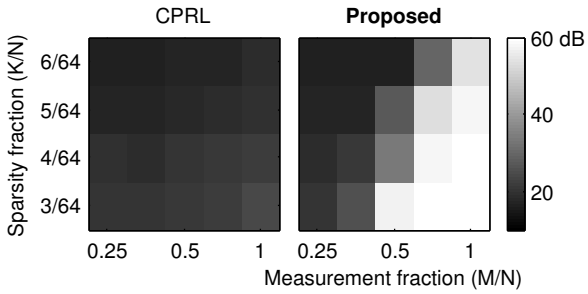

(b) 40 dB SNR AWGN + 1 outlier

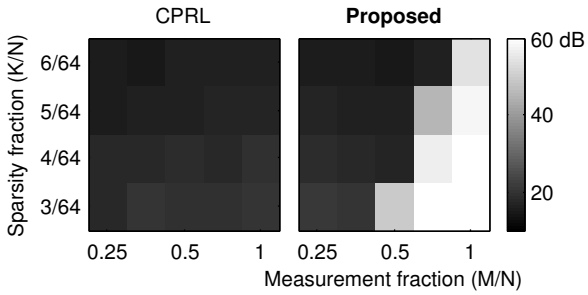

(c) 40 dB SNR AWGN + 2 outliers

Fig. 5. The median PSERs for 50 trials reconstructed using compressive matrix lifting phase retrieval (CPRL) and the proposed method for a range of measurement (M/N) and sparsity fractions (K/N), for measurements with 40 dB SNR Gaussian noise and $0-2$ outliers. Note: signal length is $N = 64$ to avoid CPRL memory issues.

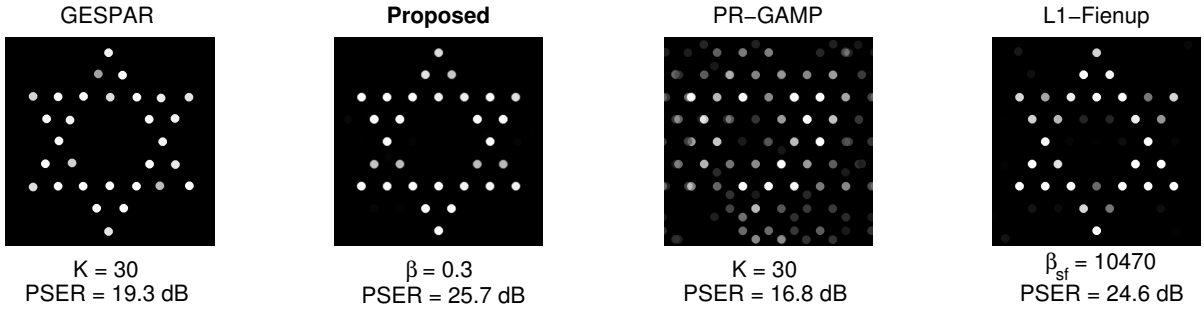

(a) 60 dB SNR AWGN + 0.001% (2) outliers

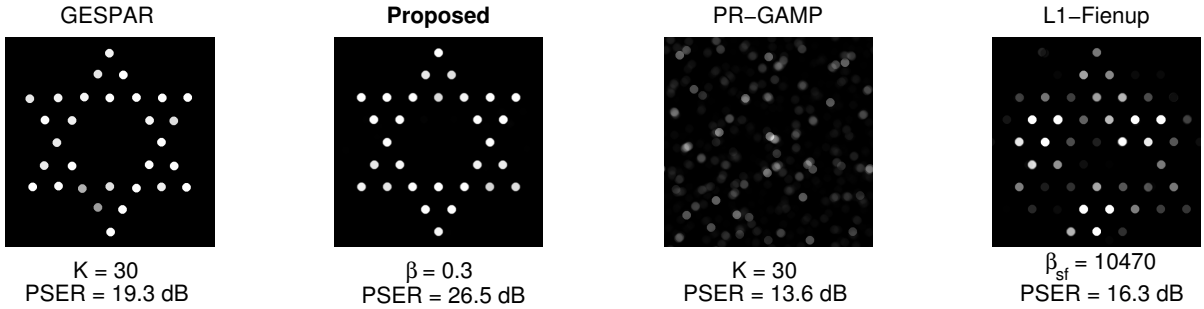

(b) 60 dB SNR AWGN + 0.01% (14) outliers

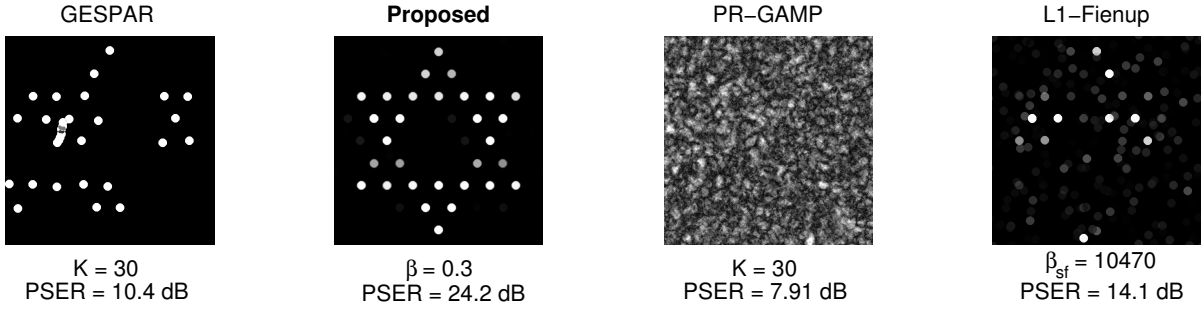

(c) 60 dB SNR AWGN + 0.1% (132) outliers

Fig. 6. The reconstruction (with regularization parameter β from the experiment in the paper – no additional tuning) for the proposed method is compared against competing methods with the optimal (true) values of β_{sf} or K. These images are shown for the 512×512-pixel star of David phantom, from $M = N/2$ measurements, with 60 dB AWGN noise and outliers ranging from 0.001% to 0.1% of the measurements.